



City Research Online

City, University of London Institutional Repository

Citation: Kanaanizade, K., Tatat, M., Guzman-Inigo, J. & Masdari, M. (2025). Passive Drag Reduction of Hyperloop Pod by Ventilation Ducts. *International Journal of Mechanical Sciences*, 299, 110405. doi: 10.1016/j.ijmecsci.2025.110405

This is the accepted version of the paper.

This version of the publication may differ from the final published version.

Permanent repository link: <https://openaccess.city.ac.uk/id/eprint/35229/>

Link to published version: <https://doi.org/10.1016/j.ijmecsci.2025.110405>

Copyright: City Research Online aims to make research outputs of City, University of London available to a wider audience. Copyright and Moral Rights remain with the author(s) and/or copyright holders. URLs from City Research Online may be freely distributed and linked to.

Reuse: Copies of full items can be used for personal research or study, educational, or not-for-profit purposes without prior permission or charge. Provided that the authors, title and full bibliographic details are credited, a hyperlink and/or URL is given for the original metadata page and the content is not changed in any way.

Passive Drag Reduction of Hyperloop Pod by Ventilation Ducts

Khashayar Kanaanizade ^a, Massoud Tatar ^b, Juan Guzman-Inigo ^c,
Mehran Masdari ^{c*}

^a College of Interdisciplinary Science and Technology, University of Tehran, Iran

^b Department of Mechanics and Maritime Sciences, Chalmers University of Technology, Sweden

^c School of Science & Technology, City St George's University of London, United Kingdom

Key words: Computational fluid dynamics, Aerodynamics, Compressible flow, Hyperloop, Drag reduction, Ventilation duct

* Corresponding author:
Email address: mehran.masdari@citystgeorges.ac.uk

Abstract

In this paper, the applicability and efficiency of ventilation duct (VD) as a novel passive drag reduction method for Hyperloop pod were investigated using 3-D numerical simulations. Ventilation duct connects the upstream and downstream parts of the pod, increasing the effective cross-sectional area and reducing drag caused by choked flow between the pod walls and the external tube. This study introduces an innovative approach to drag reduction in Hyperloop system by addressing two previously overlooked challenges. First, it overcomes the constraint of allocating central space exclusively to the passenger compartment by redirecting ducts along pod shell's boundary. Second, it enhances spatial efficiency by implementing a distributed duct configuration. For this purpose, four different design strategies along with six and eight number of ducts were proposed. The accuracy and validity of the solution were established through four distinct phases, including two comparisons with different experimental surveys, numerical research, and an assessment of mesh dependency. Results of the simulations showed that design strategy type 1 has the best performance in drag reduction. Only a minor difference in total drag was observed by changing number of ducts. It was demonstrated that VDs can decrease the total power consumption at all pod speeds with a maximum reduction of 16% obtained while occupying only 2.5% of the passenger compartment space. Comparisons of the VD method with compressor revealed that with identical removed frontal area, VDs achieve greater reductions in power consumption with less occupation of pod space.

1. Introduction

The ever-growing demand for faster, safer and more environmentally friendly transportation has driven the development of novel transportation technologies to improve performance in these criteria. Evacuated tube transportation (ETT) as a plausible solution, has attracted the attention of industrialized societies in recent decades with an increase in investigations into this system from 2011 [1-4]. The concept of the ETT was proposed for the first time by Daryl Oster in 1999 [5]. The scientific principle of the ETT is based on a Magnetic Levitated (Maglev) car-sized capsule traveling in a closed evacuated tube to reduce aerodynamic drag remarkably [6]. Years later a similar concept was presented by Elon Musk in 2013 named Hyperloop alpha. In the same manner, Musk proposed a low-pressure environment as a route for traveling while levitation in Hyperloop achieved by air bearings [7].

The construction of a sealed and partially vacuumed tube for a levitated vehicle involves a few key issues. Various critical aspects of both ETT and Hyperloop were studied and analyzed in several researches ([1], [7-11]). Musk explored the feasibility of this system in terms of technical aspects and commercial viability which highlights the importance of investigations on aerodynamic characteristics of the Hyperloop pod [7]. Investigations into the flow structure of maglev trains passing through tunnels are valuable for determining the guideway needed for the aerodynamic design of vehicles operating in a vacuum tube. Given that these studies examine key issues which are prevalent in ETT systems, such as the propagation of pressure waves within the tunnel [12-15].

However, operating in an enclosed, low-pressure environment at speeds approaching the speed of sound categorizes ETT systems as a new mode of transportation characterized by distinctive fluid dynamics phenomena. Thus, many efforts have been made to improve the understanding of flow structures around a capsule in an ETT-based system, such as Hyperloop. Several studies combined theoretical methods and numerical simulations to examine various aspects of compressible flow in transportation systems [16-21]. A 1-D theoretical model was developed to estimate pressure losses in the Hyperloop system, allowing for a cost-effective investigation of key parameters [21]. Moreover, the reliability and efficiency of a developed quasi one-dimensional model for investigations of flow characteristics in both inviscid and viscous flow was assessed [18].

A few studies have examined the factors that bring this concept closer to practical implementation. Zhang et al. proposed a divided evacuated tube design, in which the entrance and exit sections were isolated from the cruise segment, thereby reducing the aerodynamic energy consumption [22]. The impact of positioning pod stations and transfer points, which induces tube expansion and contraction, on Mach number distribution and pressure waves formation was also studied [23]. Furthermore, an experimental study investigated the impact of a branched tube on pressure waves dynamics [24]. The presence of a crack along the tube was found to induce the formation of a normal shock wave, increasing the aerodynamic drag [25].

There are also a few factors influencing the aerodynamic characteristics of the ETT-based system that were frequently overlooked in other research due to simplifications. An investigation discovered that the pod eccentricity, originating from a non-ideal pod-tube arrangement, did not significantly influence drag, although it did affect transverse force [26]. Lang et al. studied the ground effect and found that operating with a reduced suspension gap

results in an increase in both drag and downforce [27]. In contrast, Hu et al. observed no significant change in drag [28]. Further investigation revealed that an increase in the gap reduces the drag on the vehicle's head while increasing both the drag and lift on the tail [29]. The acceleration and deceleration phases of the vehicle movement were also recognized to influence its aerodynamic drag [30].

A separate group of studies has focused on analyzing the aerothermal effects and aerodynamic heating of ETT systems [31-34]. The consistent outcome from these investigations is that choking makes the thermal environment of the tube severe. A recent review on Hyperloop aerodynamics presents a similar finding, which highlights that studies exploring the contributors to aerodynamic drag of the capsule have identified choking as the dominant factor [35].

Numerous studies have investigated the effect of choking and pressure waves propagation on aerodynamic characteristics of ETT-based systems [17, 20, 36-40]. An experimental investigation indicated that pressure characteristics of the Hyperloop system can be categorized into three regimes including fully subsonic flow, transonic flow with formation of a oblique shock and fully supersonic flow [38]. The transition from regime 2 to 3 causes a reduction in the rate of drag increase [39]. The shock wave reflections at the tube exit increasing the pod drag significantly for all blockage ratios [17]. Based on the present literature , and the Kantrowitz limit theory [41] it is understood that the pod speed and the blockage ratio control the choking occurrence within the tube.

The impact of operating speed, blockage ratio (BR) or both, on aerodynamic characteristics of a tube train system has been investigated by several studies [16, 18, 42-50]. Their findings indicated that an increase in blockage ratio causes more power consumption due to a decrease in bypass cross-sectional area and generation of shock waves [43, 47]. Under constant BR conditions, it was determined that the pod drag increases with speed until a critical point is reached, where changes in the pressure wave pattern at the pod tail occur. [16, 44].

The internal tube pressure was also studied as another influential parameter on aerodynamic drag of the capsule [43, 45, 47, 51, 52]. It was discovered that the drag experienced by a vehicle traveling in a vacuum tube is linearly related to the tube pressure. [43]. Preserving the internal tube pressure on a specific level was detected as a plausible way by which total drag can be controlled [45].

Although depressurizing the internal tube airflow can significantly reduce the drag, it can be highly exorbitant and beyond a specific level more evacuation is not accessible. As a result, several active and passive drag reduction methods have been proposed by the researchers to deal with this issue. These methods can be categorized into two main groups. The first group focuses on fundamental examination of the capsule or pod geometry among which particular attention is given to shape modifications of the nose and tail-part [53-60]. It discovered that changing the tail and nose design did not have a significant impact on drag of the pod [55]. Contrary to Le results, other studies have demonstrated that changing the nose [56-58] and tail [56] shapes affects aerodynamic drag, while the tail design has a more significant influence than the nose. Increasing the pod length expanded the wake region and shifted the separation point forward [61]. Bruan et al. optimized lift generation and minimized drag by mitigating choking and delaying flow separation [62]. Geometric parameters adjustments were used to cause earlier transition near the pod nose, resulting in a separation delay and reduction of pressure drag [63]. An optimized pod model was introduced to minimize drag by reducing the pod frontal area and forcing the laminar-to-turbulent transition closer to its front. [64].

As well as geometry modifications, there are a few alternative drag reduction methods that are categorized as the second group. Examination of pressure recycle ducts (PRD) showed that they can reduce differential pressure between the head and tail of the train [65]. Adding cross passages between parallel tunnels only in some cases caused drag reduction [66]. Utilization of an axial channel had minor effect on pressure drag and the contribution of an axial channel with a radial gap caused a decrement in friction drag [67]. Different arrangements of plasma jets on train surface can cause a delay in flow separation and reduce its aerodynamic drag [68].

Throughout the review of drag reduction methods for the ETT-based systems like Hyperloop, employment of a compressor seems to work more efficiently than the rest. This method was proposed for the first time by Musk in the White paper [7]. Later Wang et al. explored the effect of adding a compressor in front of the nose, which showed an effective reduction in drag [56]. Lluesma-Rodriguez et al. discovered that the inclusion of a compressor in the pod reduced energy consumption for blockage ratios and speeds higher than 0.5 and 500 km/h respectively [69]. A new perspective for evaluation of the compressor performance was presented by Bizzozero et al., emphasizing total power consumption (P_{tot}) despite regarding only drag reduction. They found the compressor effective only at high BR and Mach numbers, while at lower speeds, it increased P_{tot} [70]. Three-dimensional numerical simulations

revealed that the compressor's efficiency dropped significantly when the tube pressure was lowered [71].

Although all previous methods were effective in reduction of drag, they have shown limited effectiveness and efficiency across varying conditions, such as different pod speeds. Despite the acceptable reduction of power consumption obtained using compressor, a number of limitations remain that are detailed in the following. As outlined in a recent review paper, none of the surveys on airflow passage within the pod body took into account how airflow passes through the body [35]. That is, they either overlooked a pathway for airflow transfer or used an overly simplified one. For instance, the research carried out by Bizzozero et al. [70] considered flow pass through a duct located at the center of the pod. However, this approach is impractical due to excessive space occupation and neglect of passenger seating. This issue can be solved by constructing a curved pathway to devote enough space for passengers or cargos, similar to the design presented by Chin et al. [11]. However, a drop in flow total head is expected by traveling a longer and turned route, negatively affecting power consumption reduction.

As highlighted in a recent review paper, none of the surveys on airflow passage within the pod body considered how airflow moves through it. That is, they either overlooked a pathway for airflow transfer or used an overly simplified one.

Moreover, pod drag is mostly influenced by the intensity of accumulated air in front of the pod and the presence of the wake [7, 46, 56, 63]. Thus, enhancing momentum of the exhaust airflow reduces the intensity of the wake which further reduces the drag. Nevertheless, direct transfer of compressed air to the rear of the pod, which would maximize energy preservation and drag reduction, is unattainable. Consequently, the actual efficiency of using a compressor is lower than that of reported in previous studies [69, 70].

Additionally, employment of a compressor imposes extra power consumption on the Hyperloop system. Therefore, an increase in total power consumption occurred in cases where the power consumption of the compressor dominated over the reduction in drag.

The limitations of the existing approaches are addressed in this research by considering a method in which power consumption is reduced while ensuring that sufficient space for passengers or cargo is available inside the pod. Investigations among drag reduction methods highlighted the potential of ventilation duct to meet these objectives. This method is inspired by an old survey in which a ventilation duct (VD) was utilized as a passive drag reduction tool

for elongated bluff bodies [72]. This approach was first introduced by G.E.A. Meier, who proposed decreasing the pressure gradient by crossing a circular duct exactly at the centerline of bluff bodies [73].

In this paper, various duct arrays on the Hyperloop pod are studied with the aim of minimizing drag while preserving the internal space of the pod with minimal space usage. Four design strategies are proposed to evaluate the significance of using a realistic method for flow transfer and to monitor how the locations of flow intake and discharge affect its efficiency. Strategies are designed by changing the intake and exhaust positions of the ducts. In addition, the impacts of duct numbers and their diameters on the quality of flow transfer are explored. Finally, the efficiency of the present method is compared with the utilization of an axial compressor.

This article is structured as follows. In Section 2, importance of the bypass space is explained. The employed numerical approach is described in Section 3. Furthermore, this section discusses how shortcomings of previous drag reduction methods are covered through the adaptation process and new designs are presented. Accuracy approval of the employed numerical solution, validation and verifications are discussed in Section 4. Results, analysis and conclusions are followed in Sections 5 and 6 respectively.

2. Bypass Space

In ETT-based systems, like Hyperloop, the bypass space, the area between the pod and the tube, plays a critical role. This issue can be explained by the Isentropic and the Kantrowitz limit. Based on isentropic relations it can be demonstrated that for flow of a perfect gas through a convergent-divergent duct (C-D duct), there is a defined cross-sectional area, named the throat, below which sonic condition is reached (i.e. Mach = 1). Whenever this state is met, choking occurs. Through isentropic relations Eq. (1) can be derived where γ is the specific heat ratio, Ma is the relative pod velocity to the speed of sound and BR is the blockage ratio that represents the ratio of the pod to tube cross-sectional area. Notably, flow behavior through the bypass space in the Hyperloop system is similar to that of a C-D duct. Therefore, Eq. (1) also can be used for the investigation of choking occurrence in the Hyperloop system. The details for the derivation of Eq. (1) are explained in Appendix A.

$$BR = 1 - Ma \left[\frac{\gamma + 1}{(2 + (\gamma - 1)Ma^2)} \right]^{\frac{\gamma + 1}{2(\gamma - 1)}}. \quad (1)$$

Under isentropic conditions, this relation is reliable. However, by emergence of shock waves, the relation of normal shock wave [41] should be employed to establish a Mach-area correlation. In the Hyperloop system, subsonic pod speeds ($Ma < 1$) result in a shock-free flow around the pod before the throat exit [48]. Under these conditions, the isentropic relation (Eq. (1)) is sufficient to determine whether the flow is choked or not. When choking occurs, flow starts to accumulate in front of the pod leading to a substantial increase in drag. Choked flow conditions are illustrated graphically in Fig. A1, provided in the supplementary material (Appendix A). To avoid choking the bypass area can be increased. However, it is not economically feasible due to the higher costs of larger tubes construction [11]. Consequently, a new approach is presented in this study to deal with the challenges of choking and space.

3. Methodology

This section primarily describes geometry of the base pod design and constraints associated with implementing the ventilation duct method. Subsequently, Section 3.2 outlines how these limitations were addressed through adaptation procedure and design parameters including design strategy and duct numbers are introduced. The computational domain and boundary conditions are described in Section 3.3. Details of the numerical scheme, basic assumptions and selection of the turbulence model is presented in Section 3.4. The last section expresses the sizing strategy and refinement approach used for mesh generation at different stages of this study.

3.1. Base Design

A preexisting model introduced by Bizzozero et al. [70] was chosen as the base pod design. Using this model allows us to compare the efficiencies of a compressor and VDs in terms of power consumption and space occupation. Tube radius is set at 1.1 m matching the dimensions of the EuroTube design [74]. As the present study focuses on pod drag reduction, particularly in choked flow conditions, blockage ratio of 0.6 is chosen because it allows choking to occur across a wide range of free-stream Mach numbers while also including a non-choked case. Thus, ventilation duct efficiency, is evaluated under both choked and non-choked conditions. The pod radius is determined to be 0.85 m using Eq. A.3, provided in the supplementary material (Appendix A). Other parameters of the geometry are calculable due to their relations with the pod radius [70].

The implementation of the VD method in Hyperloop design faced two important restrictions. One key issue was that the ventilation duct could not pass directly along the

centerline of the Hyperloop pod, as intended in its original concept [73], and depicted in Fig. B1, provided in the supplementary material (Appendix B). The second challenge was the size of the VD. Various values for the vented area were considered in previous studies [75, 76], where 2.25% and 2.78% of bluff bodies frontal area were more common. As a quantity between former studies, 2.5% of the pod frontal area (A_{pod}) was admitted. Given that A_{pod} is 2.28 m^2 (based on calculated radius of 0.85 m), the VD diameter was determined to be 27 cm. However, this size is disproportionately large for a pod with a 1.7 m diameter, occupying 10% of the passenger compartment.

3.2. New Design

To overcome the first limitation, the ducts were proposed to be routed through the pod walls. In this way, only a thin layer of the pod walls was designated for their passage. The second restriction was solved by using multiple ducts with smaller diameter. These solutions lead to designs with multiple ducts positioned along the edge of the pod hull, effectively isolating the passenger section from the flow transfer line. In the present study, the mid-part of the pod was regarded as the passenger section.


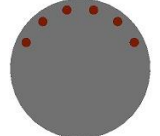

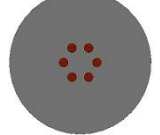

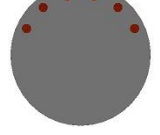

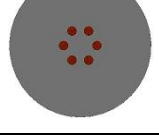
The effective position for VDs inlet is towards the stagnation point where flow has the maximum total pressure. As well as this, the wake structure is expected to be disrupted more effectively when the discharged flow is against the center of the wake. As a result, simulations of some cases, in which ducts are directed from the stagnation point to the wake center, were suggested to investigate the efficiency of displacing the duct inlets and outlet. These three steps are referred to as the adaptation procedure in this study.

The third suggestion of the adaptation procedure results in the generation of four design strategies based on radial distance (R) of the duct inlets and outlet from the centerline of the pod. Two values were considered for their distances including 0.73 m as the maximum and 0.2 m as the minimum distance. By permutation of these configurations for each of the duct inlets and outlet, four design strategies are produced as summarized in Table 1. The number of the ducts (N_d) is set to two arbitrary values which are 6 and 8. Thus, a total of eight distinct duct configurations were proposed by applying each design strategy (DS) for both 6 and 8 ducts. Side and frontal views of all four design types for $N_d = 6$ are shown in Table 2. Each configuration is labeled with two numbers. The first number indicates the number of the ducts and the second refers to the design type listed in Table 1.

Table 1. Design strategies for ducts inlet and outlet. The maximum and minimum indicate the radial distance of 0.73 and 0.2 from centerline of the pod respectively.

Design Strategy	R-coordinate of inlet	R-coordinate of outlet
Type 1	Maximum	Maximum
Type 2	Minimum	Maximum
Type 3	Maximum	Minimum
Type 4	Minimum	Minimum

Table 2. Side and frontal view of the pod with 6 number of ducts in 4 design strategies. The configurations are labeled with two numbers: the first one indicates the ducts number and the second represents the design strategy, as listed in Table 1.

Configurations	Side view	Frontal veiw
Design 6.1		
Design 6.2		
Design 6.3		
Design 6.4		

The diameter of the VDs was calculated based on the removed frontal area of the pod, as explained in Section 3.1. Consequently, diameter of each duct for $N_d = 6$ and 8 are 0.0475 m and 0.055 m respectively. Ducts are spaced equally from each other and their distance is determined by the angle θ , as shown in Fig. 1. In this study, θ was assumed to be a constant value of 25.7° .

3.3. Computational domain and boundary conditions

As depicted in Fig. 1 the whole geometry is symmetric with respect to the x-y plane (i.e. $z = 0$). As a result, three-dimensional (3-D) symmetrical simulations were held for the rest of the research. The length of the domain is 40 m. For $BR = 0.6$, the pod length is about 9 m and the downstream region of the pod is about 21 m. This downstream length was discussed to be

sufficient for accurate calculations around the pod [70]. The pressure and temperature of the air inside the tube was set 0.1 atm and 300 K respectively.

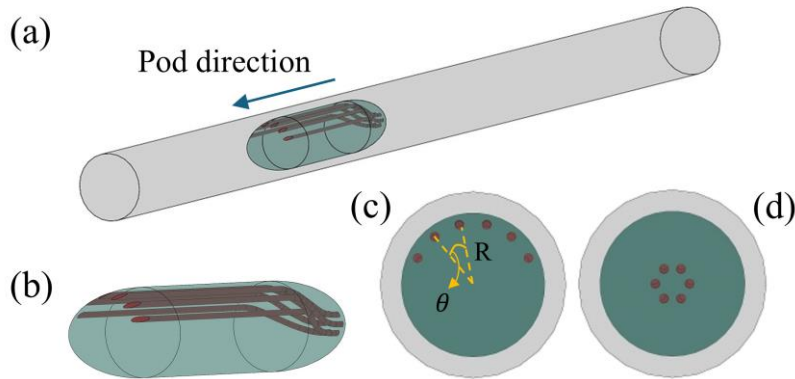


Fig. 1. Three-dimensional view of the (a) pod, tube and (b) pod design 6.3. (c), (d) Cross-sectional views of the front and rear of the pod and tube, with a removed area equal to 2.5% of the pod's frontal area. The diagrams indicate the radial distance of the duct inlets and outlet from the pod centerline (R) and the angular spacing between them (θ).

In Fig. 2 computational domain and boundary conditions are shown. The moving wall boundary condition was used for the tube wall. The mass flow rate was imposed for the inlet. At the outlet, the static pressure was used to conduct solution for pressure field calculation. No slip conditions were imposed on the walls of the tube, pod and VDs.

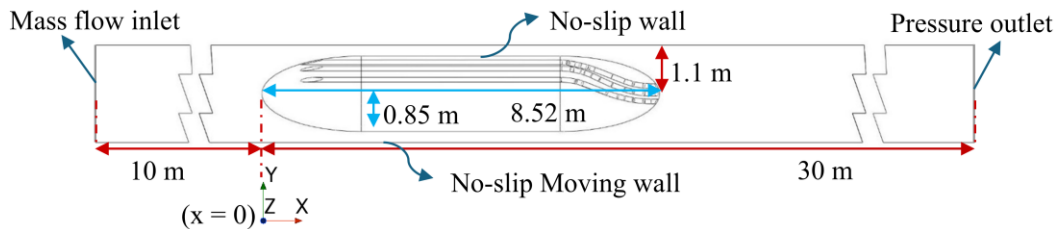


Fig. 2. Computational domain and boundary conditions for design 6.3. The shown geometry and boundary conditions are illustrated on a cross-section of the x - y plane. The same domain and boundary conditions are applied to all other design configurations.

3.4. Numerical method

The Navier-Stokes equations were solved based on finite-volume method using the commercial CFD code STARCCM+. The second-order upwind scheme was used for discretization and the coupled flow solver with pseudo-time marching approach was employed. The steady-state assumption was taken following the outcomes of [46, 48]. Since the flow Mach number in all simulations is locally higher than 0.3, the fluid is assumed to be an ideal gas to account for compressibility. Sutherland's law was used for the determination of the air dynamic viscosity [37, 53]. Roe's flux-difference splitting scheme [77] is used for the evaluation of the inviscid flux. The Reynolds number (Re) is calculated based on the relation

of $Re = \rho v L / \mu$ in which ρ (density) is derived from the equation of state, v is the pod velocity in each case, μ is the dynamic viscosity of air. The characteristic length (L) is defined as the hydraulic diameter ($D_h = D_t - D_p$) where D_t and D_p are tube and pod diameters respectively. By these considerations, Re ranges from 2.2×10^5 to 9.9×10^5 . In this range flow is fully turbulent.

Three different turbulence models were employed to examine their capability on more realistic flow field computation compared to the experimental data. They include realizable $k - \varepsilon$ two-layer [78, 79] (RKE2L), elliptic-blending lag $k - \varepsilon$ [80] (EBLKE) and shear stress transport $k - \omega$ [81] (SST KO). Among the recommended models, the EBLKE model had the least error in the validation phase two (presented in Section 4.3) and had acceptable results in both the other validation phase (described in Section 4.2) and verification phase (presented in Section 4.4).

3.5. Meshing strategy

An identical mesh setup was used for all designs. Prism layer meshes were used for the regions close to the pod and duct walls and hexahedral cells for the regions far from the pod. A multi-level refinement approach was employed, refining the cells of five regions: the inner part, outer parts 1 and 2, the wake region, and the ducts area, as shown in Fig. 3.

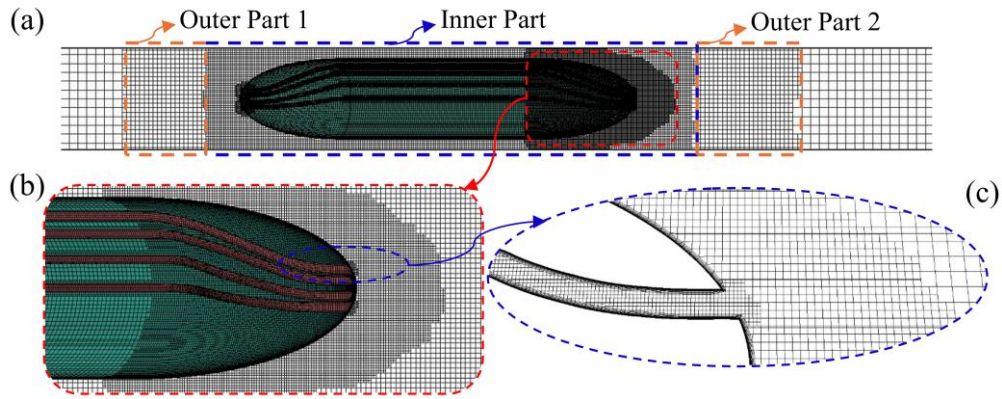


Fig. 3. Mesh visualization of the refined volumes around pod design 8.4 on the symmetry plane ($z = 0$) showing: (a) the inner part (cells are halved twice), outer part 1 and 2 (cells are halved one time), (b) wake region (cells are halved three times), (c) the internal region of the top VD (cells are halved four times).

The cell sizes decrease by half with each level of refinement as one moves from the inlet and outlet towards the pod location. Using a mesh dependency analysis, described in Section 4.1, a base size of 0.19 m for the region far from the pod was chosen for the rest of the simulations. The prism layer mesh was generated with a first cell height of 0.015 mm, stretch factor of 1.3 and 22 layers.

4. Validation and Verification

In this section the validity of the employed numerical scheme is established through four distinct validation and verification phases. Section 4.1 presents the verification of mesh independence for design 8.4 at Mach number of 0.4. The first validation phase, described in Section 4.2, demonstrates the accuracy and validity of compressible flow calculations. Section 4.3 discusses the validation against an experimental study conducted to assess the accuracy of the numerical solution within the ducts, as duct diameters are significantly smaller than diameter of any conduits in the domain. Finally, verification of the base pod design is detailed in Section 4.4.

4.1. Mesh independence analysis

This verification phase studied independence of the computational mesh for design 8.4 at Mach number of 0.4. Three mesh configurations were considered namely coarse, medium and fine for this aim. To refine the meshes, the size of the cells in every zone is halved, as detailed in Table 3. Since drag reduction is the primary goal of this study, the variation in the drag coefficient (C_d) was regarded for this analysis.

Table 3. Details of mesh sizes and calculated C_d for mesh independence verification for design 8.4 at $Ma = 0.4$.

Mesh density	Base cell	Outer parts 1 & 2	Inner Part	Ducts	Wake	Total number	C_d	Differences
Coarse	0.38 mm	0.19 mm	0.095 mm	0.0304 mm	0.0475 mm	0.65 million	9.35	3.09%
Medium	0.19 mm	0.095 mm	0.0475 mm	0.0152 mm	0.0237 mm	2 million	9.1	0.33 %
Fine	0.095 mm	0.0475 mm	0.0237 mm	0.0076 mm	0.0119 mm	9 million	9.07	-

The refinement length for the wake zone was assessed by examining four different values (0.3, 0.6, 0.9, and 1.2 m) at $Ma = 0.2, 0.4, 0.6$, and 0.8 . A maximum difference of 0.5% was observed for lengths beyond 0.6 m, confirming that 0.6 m is sufficient for reliable calculations. The drag coefficient with the fine mesh changes so slightly in comparison to the medium one. Thus, the medium mesh was used to diminish computational costs while keeping the accuracy of calculations. Reliable calculation for near wall region was ensured by keeping the dimensionless wall distance parameter (y^+) close to 1.0. Distribution of y^+ for walls of the pod, tube and the top VD are separately plotted in Fig. 4.

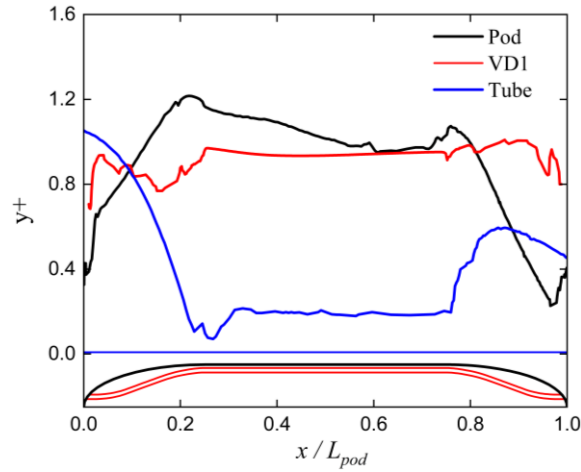


Fig. 4. Distribution of the dimensionless wall distance parameter (y^+) on walls of the pod, tube and top VD for design 8.4 at a Mach number of 0.4. A schematic of the geometry is shown at the bottom of the graph, below the zero mark on the y-axis.

4.2. Validation with experimental test phase one

The computational approach was validated by simulating an experimental test [82] involving various compressible flow phenomena, such as the generation and reflection of shock waves within a confined channel, which is a critical feature of the flow structure in the Hyperloop system. Test section of the experiment is a rectangular channel where a wedge is located at the bottom wall. The computational domain and boundary conditions are shown in Fig. 5(a). As the whole domain was symmetric respect to the x-y plane ($z = 0$), computations were done for half of the domain by employing a symmetry boundary condition.

The validation was conducted quantitatively by comparison of the non-dimensional pressure distribution on bottom and top wall of the channel, as shown in Fig. 5(c-d). The calculation results for both the bottom and top surfaces show good agreement with the experimental data, accurately capturing most data points and correctly following the trend of pressure variation. Moreover, a qualitative comparison was made to show the accuracy of locations of the captured shock waves and their reflections which is demonstrated in Fig. 5(b). The locations of the shock waves and their reflections are calculated with high accuracy, with only minor deviations. Furthermore, both quantitative and qualitative comparisons were made with the 2D simulation results by Li et al. [82]. While the qualitative features are comparable, the present results show noticeably better quantitative agreement with the experimental data than those reported by Li et al. To ensure that numerical discrepancies were not caused by mesh resolution, a mesh independence analysis was conducted for this validation case. The methodology and results are provided in the supplementary material (Appendix B). Based on this validation, the accuracy

of the employed numerical scheme in calculating compressible flow with shock wave formations is demonstrated.

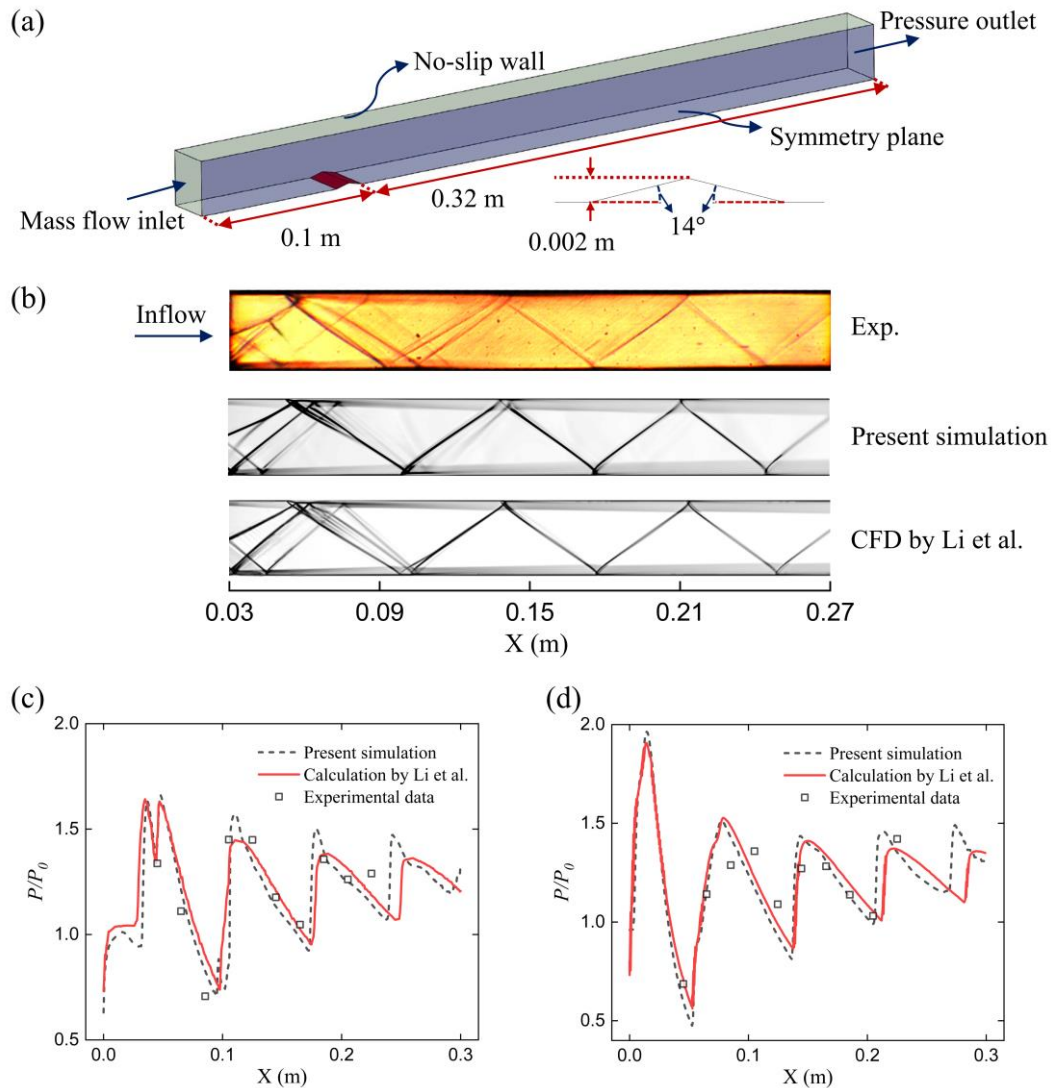


Fig. 5. Validation phase one: comparison with experimental test of a compressible flow inside a confined channel [82]. (a) The computational domain and boundary conditions of the numerical model. (b) Qualitative comparison of shock wave locations and their reflections between schlieren images from experimental test, the CFD results by Li et al., and the present simulation. (c) Comparison of the non-dimensional pressure distribution along the bottom and (d) top surfaces of the channel among the experimental data, the calculations by Li et al., and the present simulation.

4.3. Validation with experimental test phase two

In the second phase of validation, the accuracy of the numerical scheme used for calculations inside the ducts was confirmed. To the best of the authors' knowledge, no experimental study has investigated a high-compressible flow under Hyperloop pod conditions involving a ventilation duct. Therefore, a case investigated by Grosche et al. [76], covering the whole range of Reynolds numbers studied in this research, was selected for this purpose. Details of the geometry are presented in Fig. C1, provided in the supplementary material

(Appendix C). A three-dimensional simulation was conducted in which the vented body was positioned in a rectangular channel with the same cross-sectional area as the wind tunnel test section. The boundary conditions and computational domain are shown in Fig. 6(a). Three turbulence models (RKE2L, EBLKE and SST KO) were employed to evaluate their accuracy in calculation of drag coefficient (C_d) of the vented bluff body. To eliminate mesh resolution as a potential source of numerical variations, a mesh independence study was also conducted for this phase of the validation, with details provided in the supplementary material (Appendix C). Fig. 6(b), shows the comparison between the results of the experiment and three numerical simulations with different turbulence models are presented. The EBLKE model provided the least error in the whole range with maximum error of 13% while for RKE2L and SST KO they were 21% and 38% respectively. Thus, the EBLKE model was used for the rest of the analysis.

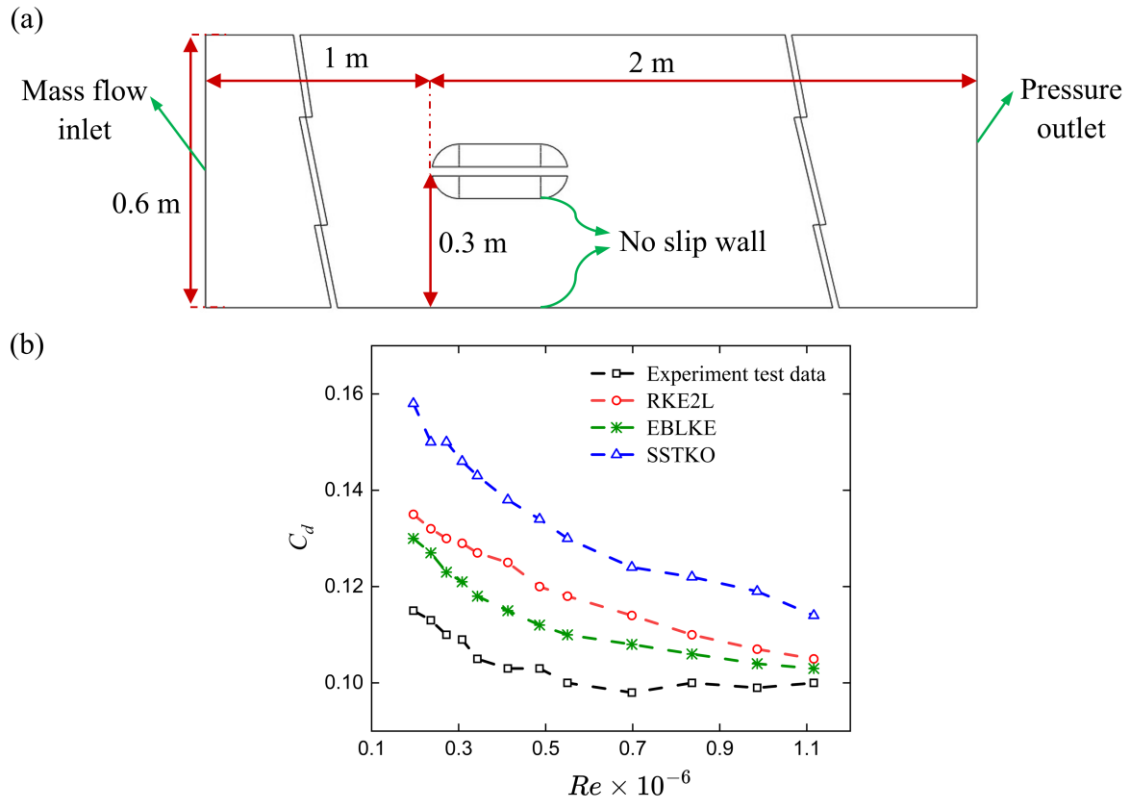


Fig. 6. Validation phase two: comparison with experimental test of a bluff body with ventilation duct [76]. (a) The computational domain and boundary conditions of the numerical model. (b) Comparison of the drag coefficient (C_d) between the experimental data and the present numerical results, obtained using three different turbulence models (as described in Section 3.4), over a wide range of Reynolds numbers (Re).

4.4. Base model verification

As explained in Section 3.1 the base pod model introduced by Bizzozero et al. [70] was chosen to make a comparison between the compressor and ventilation ducts (VDs) efficiencies.

Therefore, the results of the present study and simulations of the previous research were compared over a wide range of Mach numbers to verify the Hyperloop base pod design. The previous study conducted two-dimensional axisymmetric simulations using the realizable $k - \varepsilon$ turbulence model while the present research studied the flow field around the pod in a three-dimensional symmetric configuration employing the elliptic-blending lag $k - \varepsilon$ model. Fig. 7 compares drag coefficient (C_d) calculations from both studies. Their difference is less than 5%, demonstrating the validity of the chosen numerical approach for the base pod design simulations.

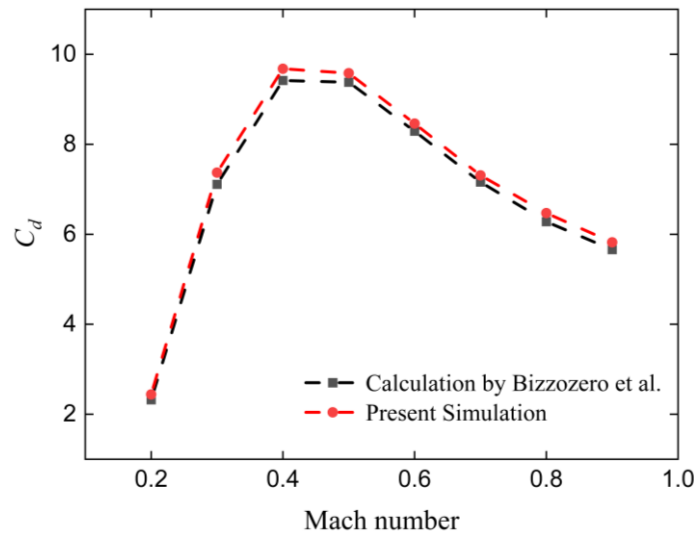


Fig. 7. Verification of the numerical scheme for the base model of the Hyperloop pod (i.e., the design without VDs) at BR = 0.6. The drag coefficient (C_d) calculated from the present simulation using the EBLKE turbulence model is compared with the results of a previous study employing the RKE2L model [70]. The turbulence models are described in Section 3.4.

5. Results and Discussion

This section focuses on the effects of new designs on drag reduction and modifications in flow structure. Section 5.1 presents an analysis of the flow structure around the base pod design (i.e., the pod without VDs) and identifies the key factors contributing to drag. The impacts of design strategies, duct numbers and diameter are studied in Sections 5.2 and 5.3. Reasons for the occurrence of maximum drag reduction at critical Mach number are presented in Section 5.4. Ultimately, the VDs efficiency in reducing total power consumption is compared to that of a compressor in Section 5.5.

5.1. Base pod design

While the flow structure around the base model has been examined in several studies [16, 39, 70], this section introduces features that demonstrate the potential of the VD method as a

drag reduction approach in the Hyperloop system. The Hyperloop pod drag is significantly affected by flow choking [70]. To describe its impact on aerodynamic drag, three flow regimes were defined based on the pod speed [16, 39]. The corresponding speed ranges vary with the blockage ratio, as determined by the isentropic limit. Accordingly, this study employs the critical Mach number (Ma_{cr})—the free-stream Mach number at which flow choking occurs—as a variable to distinguish between the different flow regimes. Based on Eq. (1) and considering a blockage ratio of 0.6, the critical Mach number is 0.24. However, due to the presence of a compression wave formed ahead of the car, the actual critical Mach number is slightly higher, at 0.26 [48].

For $Ma < Ma_{cr}$, the flow around the pod remains fully subsonic, and no shock waves are formed. In this regime, drag is primarily caused by the pressure drag at the pod tail due to wake formation. For speeds exceeding Ma_{cr} , the flow regime is characterized by the formation of shock waves. Specifically, the presence of a normal or oblique shock on the pod tail defines the second regime. In this regime, the mass flow rate (\dot{m}) through the bypass space reaches its maximum due to flow choking. Consequently, excess mass flow accumulates ahead of the pod, increasing drag compared to non-choked conditions. Moreover, as in the subsonic regime, wake formation continues to significantly contribute to pressure drag.

The last flow regime is characterized by the propagation of oblique shock waves downstream of the pod, where the interactions between reflected shock waves and the trailing vortical structures disrupt the vortex formation at the pod tail, resulting in a diminished wake region. Therefore, for cases in this flow regime, the pressure build up ahead of the pod becomes the dominant contributor to pod drag. In the present study, this flow regime was observed at Mach numbers of $Ma \geq 0.6$. A representation of the flow structure for each flow regime is shown in Fig. D1, provided in the supplementary material (Appendix D).

Given the function of ventilation duct, it can effectively reduce drag across all flow regimes. In supersonic regimes (i.e. $Ma \geq Ma_{cr}$), VDs can remove a portion of the accumulated air in front of the pod, thereby lowering the upstream pressure, which contributes most significantly to the total drag. In subsonic regimes (i.e. $Ma < Ma_{cr}$), VDs can increase the pressure in the wake region by transferring upstream, thus reducing the tail pressure drag.

Fig. 8 shows the pressure coefficient profile along the base pod model and design 6.1, illustrating how the VDs modify the pressure field along the pod. A pressure reduction ahead of the pod is caused by the employment of VDs, as shown in Fig. 8(b) (blue box). Additionally,

the flow discharged from the duct outlets increases the pressure over the tail and further downstream, as depicted in Fig. 8(c) (red box). The strength of the oblique shock also decreases due to the reduced pressure difference across the shock.

Fig. 9 illustrates the effect of VDs on circumferential pressure field both upstream and downstream of the pod by comparing pressure coefficient distribution on cross-sectional planes located at $x = -0.06, 0.06, 0.94$ and $1.06 L_{pod}$. A comparison between Fig. 9(c) and Fig. 9(g), as well as between Fig. 9(d) and Fig. 9(h), reveals a reduction in the pressure field ahead of the pod due to the use of VDs. Likewise, comparisons between Fig. 9(e) and Fig. 9(i), and between Fig. 9(f) and Fig. 9(j), indicate a corresponding pressure increase downstream of the pod. As expected, the VDs reduce the pressure upstream of the pod by drawing flow from this region and redirecting it toward the wake, where it is low-pressure. This redistribution of flow increases the pressure in the wake and consequently reduces the overall pressure gradient between the nose and tail of the pod, resulting in a significant drag reduction.

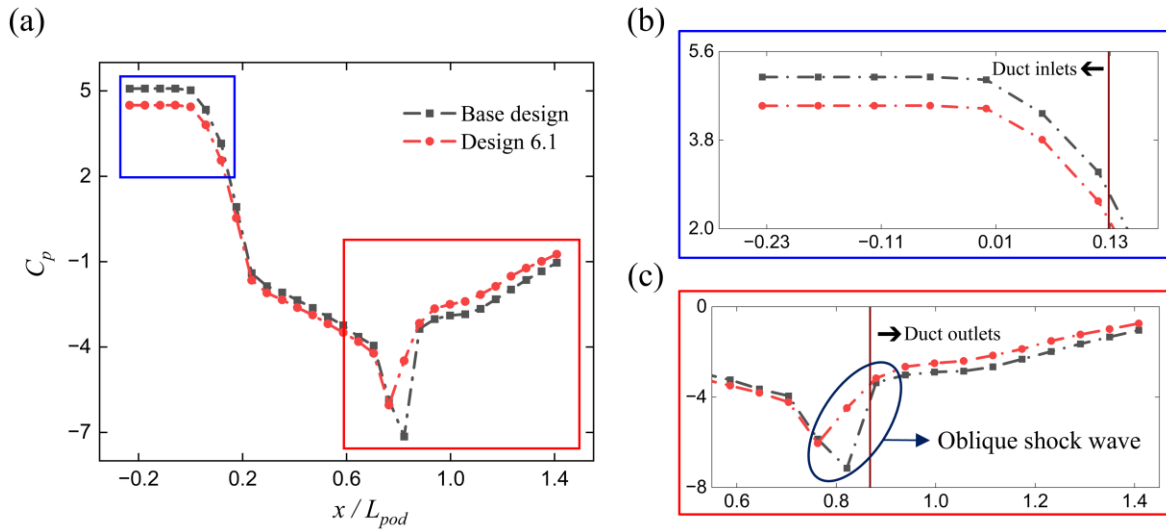


Fig. 8. (a) Comparison of the pressure coefficient profile upstream, downstream, and along the pod between the base design (i.e., without VDs) and design 6.1 at $Ma = 0.3$. Model identification is labeled as referenced in Table 2. (b) Magnified view showing duct inlets positions and the effect of VDs on the pressure field ahead of the pod (blue box). (c) Magnified view showing the positions of duct outlets and the impact of VDs on the downstream pressure (red box), indicating a reduction in shock strength due to the use of VDs.

5.2. Effect of design strategies

The reduction of drag obtained by each new design for a wide range of Mach numbers is reported in Table 4. The results are divided into two categories based on the number of ducts (six and eight). Within each group, DS type 1, i.e. designs 6.1 and 8.1, achieved the largest reductions in drag compared to other design strategies. Since similar findings appear across

design strategies in group 2 (i.e. designs with $N_d = 8$), the impact of design strategies on drag reduction is analyzed only for group 1.

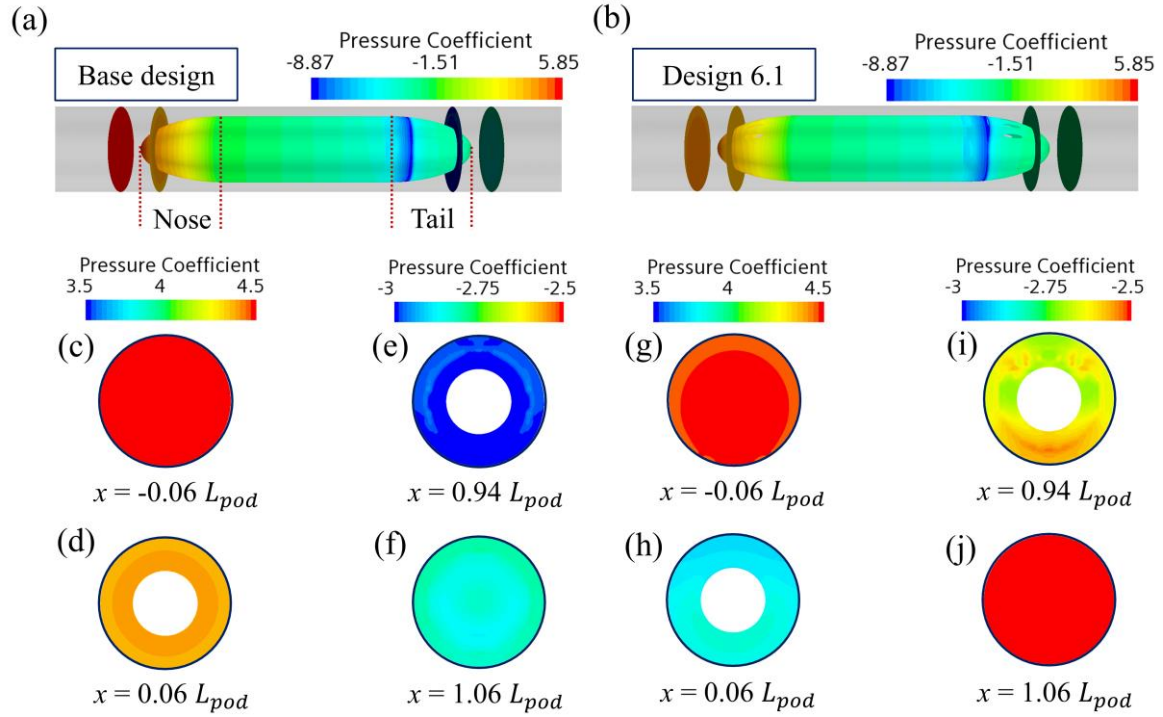


Fig. 9. Pressure coefficient comparison between (a) the base model and (b) design 6.1 along the pod at $Ma = 0.3$. Model identifiers are listed in Table 2. Pressure coefficient distributions at various cross-sectional planes are shown for (c–f) the base design and (g–j) design 6.1. The first two planes, located ahead of the nose and at the nose of the pod, are positioned at longitudinal distances of -0.06 and $0.06 L_{pod}$ from the pod nose respectively. The third and fourth planes, situated at the pod tail, are located at 0.94 and $1.06 L_{pod}$ respectively.

Table 4. Calculated drag reduction rate for different configurations of VDs and Mach numbers (%)

Design Type/ Mach Number		0.2	0.3	0.4	0.5	0.6	0.7	0.8	0.9
6 Ducts	Design 6.1 R_{in} : Max, R_{out} : Max	-5.8	-12.2	-7.4	-6.6	-5.2	-5.1	-5.3	-5.3
	Design 6.2 R_{in} : Min, R_{out} : Max	-4.7	-10.7	-6.8	-5.9	-4.5	-4.5	-4.6	-4.6
	Design 6.3 R_{in} : Max, R_{out} : Min	-4.5	-11.0	-7.0	-5.9	-4.7	-4.6	-4.7	-4.7
	Design 6.4 R_{in} : Min, R_{out} : Min	-3.2	-9.7	-6.3	-5.4	-4.1	-4.1	-4.1	-4.2
8 Ducts	Design 8.1 R_{in} : Max, R_{out} : Max	-5.1	-11.5	-6.9	-6.0	-4.9	-4.8	-5.0	-4.9
	Design 8.2 R_{in} : Min, R_{out} : Max	-3.7	-10.1	-6.3	-5.4	-4.4	-4.3	-4.4	-4.3
	Design 8.3 R_{in} : Max, R_{out} : Min	-3.3	-10.4	-6.6	-5.7	-4.3	-4.3	-4.2	-4.3
	Design 8.4 R_{in} : Min, R_{out} : Min	-2.5	-9.1	-5.9	-5.1	-3.9	-3.9	-3.9	-3.8

To figure out why DS type 1 has achieved greater drag reduction, it is preferable to study the effect of each strategy on drag variations for each part of the pod individually. Fig. 10 illustrates the ratio of pressure drag coefficient (C_{dp}) for each part on pod total drag coefficient (C_{dt}) for design 6.4. The results reveal that the nose and tail pressure drag contributed significantly more to pod total drag compared to the pressure drag of the mid-part and VDs, which had a minor impact. As a result, the rest of the study focuses on pressure drag variations of the nose and tail to evaluate the effects of the new designs on pod total drag.

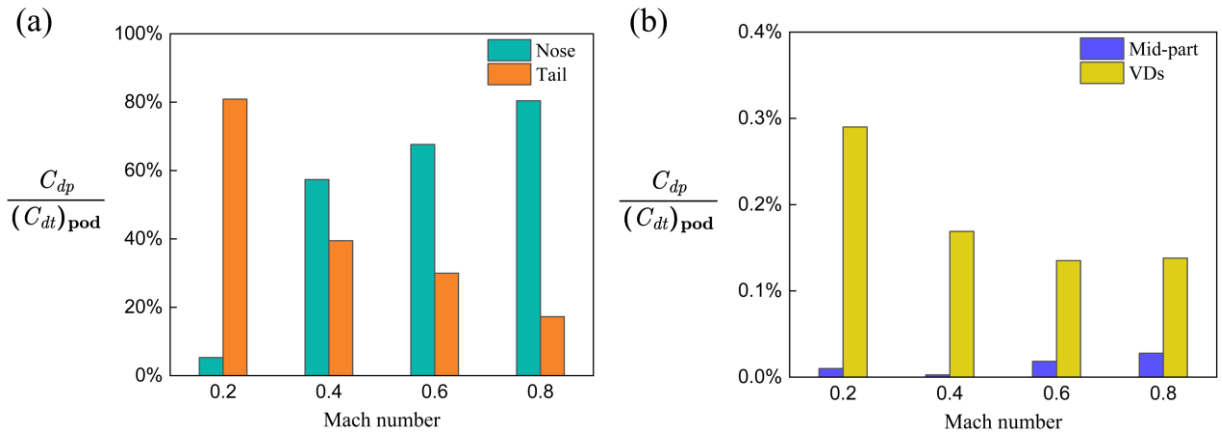


Fig. 10. Ratio of pressure drag contribution from different parts of the pod—including (a) the nose and tail, and (b) the mid-section and ventilation ducts (VDs)—relative to the total drag of the pod for design 6.4 across various Mach numbers. The mid-section corresponds to the passenger compartment of the pod. Model configuration is identified as design 6.4, with details provided in Table 2.

Fundamentally analyzing, in the Hyperloop system pressure drag is significantly affected by the wake [46] and accumulated air as a result of choking [7]. The wake influences the tail drag while the second source impacts the nose drag. As shown in Fig. 10, the variation of nose and tail drag contributions with increasing Ma follows a typical trend. Additionally, for Ma = 0.2, air accumulation does not occur, as explained in Section 5.1, and a larger share of the total drag originates from the wake. Consequently, the variation in pod drag for cases in the subsonic flow regime (i.e., $Ma < Ma_{cr}$) can be explained by investigating the influence of VDs on the tail pressure drag.

5.2.1. Nose pressure drag variation

Fig. 11(a) illustrates that DS type 2 and 4 (i.e. design 6.2 and 6.4) which draw the flow from tip of the nose, caused a lower reduction in pressure drag of the nose compared to DS type 1 and 3 (i.e. design 6.1 and 6.3). The variations on pressure distribution over each part of the pod, caused by different design strategies directly correlates with the change on pressure drag of each part. Thus, impact of each design on pressure distribution over the pod nose are compared

in Fig. 12. Designs 6.2 and 6.4 result in a higher pressure reduction only in a small region at the nose tip, adjacent to their duct inlets, as shown in Fig. 12(b). However, this reduction is not comparable to that achieved by designs 6.1 and 6.3, particularly within the range $0 < x/L_{pod} < 0.12$ which corresponds to half the nose length. This confirms the expectation from the VDs described in Section 5.1, as designs with a higher capability to reduce pressure upstream of the pod result in a greater reduction in pressure drag. Furthermore, Fig. 12(d) shows that although the duct inlets in designs 6.1 and 6.3 are not toward the stagnation point, they still cause a pressure drop at the nose tip, similar to the other two designs. This analysis reveals that the reduction in nose pressure drag is not solely dependent on the position of the duct inlets.

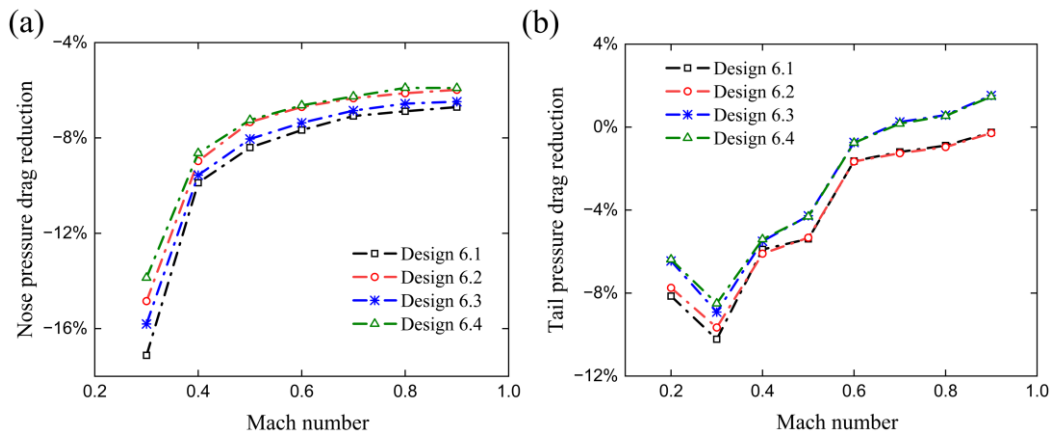


Fig. 11. Pressure drag reduction at (a) the nose and (b) tail of the pod by different design strategies across various Mach numbers. The comparison highlights the effect of each individual design strategy and illustrates variation of VDs efficiency with increasing Mach numbers. Design models incorporate 6 ducts using DS types 1-4. Model identifications are provided as in Table 2.

As discussed in Section 5.1, air accumulation resulting from choking contributes significantly to the nose pressure drag in the supersonic flow regime (i.e., $Ma \geq Ma_{cr}$). Therefore, it can be inferred that under choking conditions, redirecting more airflow away from the front of the pod leads to a greater reduction in nose pressure drag. To understand which DS has taken more of the upstream flow, analyzing the variation in momentum coefficient (C_μ) at the duct inlets is advantageous, since it directly correlates with pressure drag in flow control methods like suction and injection [83]. It is defined as Eq. (2), where \dot{m} is the mass flow rate, v is the velocity, ρ is the density of air inside the tube, U is the free-stream velocity and A_{ref} represents the frontal area of the pod. Total values of momentum coefficient at duct inlets in each DS are compared in Fig. 13(a). Higher values of momentum was captured by design 6.1 at all Ma, in which VDs are positioned based on DS type 1, i.e., it has demonstrated superior

capability in natural transfer of airflow from the pod front. Hence, it has brought a higher reduction of pressure drag in comparison to other design strategies.

$$C_\mu = \frac{\dot{m}v}{0.5\rho U^2 A_{ref}}. \quad (2)$$

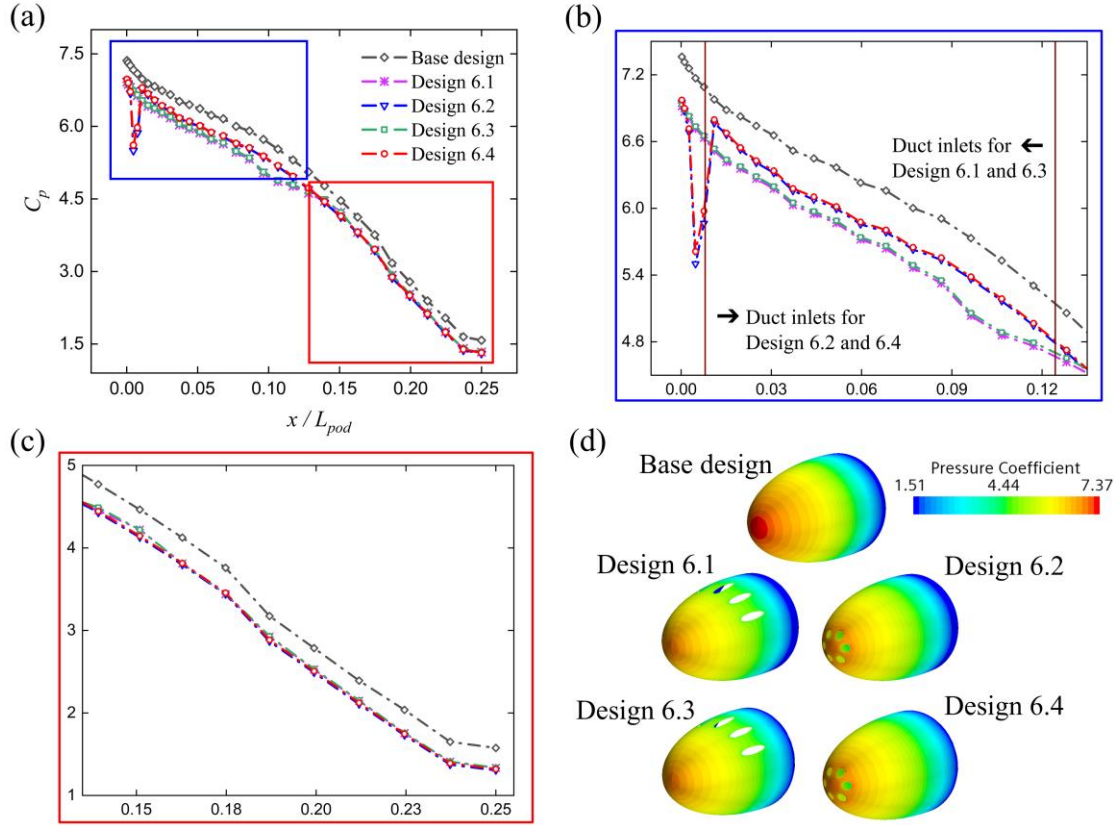


Fig. 12. (a) Quantitative comparison of pressure coefficient distribution on the pod nose at $Ma = 0.4$, between the base design and four design strategies, each featuring 6 ducts. The configurations are labeled as referenced in Table 2. (b), (c) Magnified views of the pressure coefficient distributions indicated by the blue and red boxes in (a). (d) Qualitative comparison of pressure distribution over the nose surface, highlighting changes in the stagnation point caused by each DS.

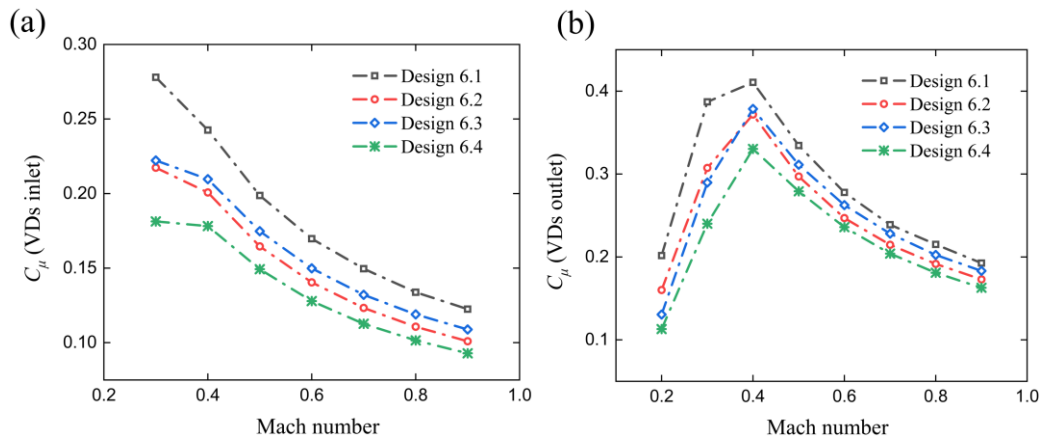


Fig. 13. Comparison of momentum coefficients (C_μ) at VD (a) inlets and (b) outlets for various design strategies across a range of Mach numbers, indicating the effectiveness of each DS in facilitating flow transfer through the VDs, with higher momentum coefficients indicating improved performance. Model configurations are specified as listed in Table 2.

Fig. 14 shows a precise view of the flow structure through the top VD. In DS types 1 and 3, ducts are aligned streamwise, allowing direct airflow entry and preventing flow circulation, as shown in Fig. 14(b). In contrast, DS types 2 and 4 induced deflection in the intake flow, causing an adverse pressure gradient near the wall, which leads to flow recirculation and separation at the VD inlets, as depicted in Fig. 14(d), (e), (f). The separation caused the passageway to narrow, decreasing the mass flow rate (\dot{m}) at the inlet of VDs. For this reason, momentum of the intake flow with these design strategies was less than the others.

5.2.2. Tail pressure drag variation

Pressure drag reduction of the tail made by different design strategies is depicted in Fig. 11(b), showing distinct patterns compared to the nose. Except $Ma = 0.2$ and 0.3 , designs 6.1 and 6.2 approximately have the same outcomes, as do designs 6.3 and 6.4, indicating that designs involving the same position for duct outlets have an analogous influence on the tail pressure drag.

To elucidate how design strategies altered structure of the wake region, their influence on this area are compared in Fig. 15. The visualization of wake disruption by VDs aligns with the findings in Fig. 11(b), demonstrating that designs 6.1 and 6.2 have similar effects, particularly in wake shrinkage observed in both x - y and y - z cross-sectional planes. Flow injection by VDs at the top area of the wake, increased flow momentum over the tail facilitating streamwise flow continuation instead of recirculation. In contrast, designs 6.3 and 6.4 achieved limited reductions in wake width with contraction confined to the region that injected flow reached, marked by the velocity line $u = 0$, u is the velocity component in x -direction, at the wake center. Although discharging flow in that area increased local pressure and reduced the pressure gradient, still there is a thick wake downstream of the pod. Therefore, the resulting reduction of C_{dp} for the tail caused by designs 6.3 and 6.4 was lower than the other configurations.

The change in wake length is another noticeable point that is caused by utilization of VDs. Wake length for different designs is compared by the length of the velocity line ($u = 0$) shown by the white line in Fig. 15. All design strategies shorten the wake length, although for designs 6.3 and 6.4, it is slightly more elongated in comparison to the others.

Fig. 11(b) also shows a sharp decrease in the rate of pressure drag reduction at the tail for $Ma \geq 0.6$. As explained in Section 5.1, oblique shock waves and their reflections disrupt the wake region in the third flow regime, which is established for free-stream Mach numbers

exceeding 0.6. Thus, the absence of a low-pressure area at the tail in this regime reduces the VDs efficiency in pressure drag reduction for this part of the pod.

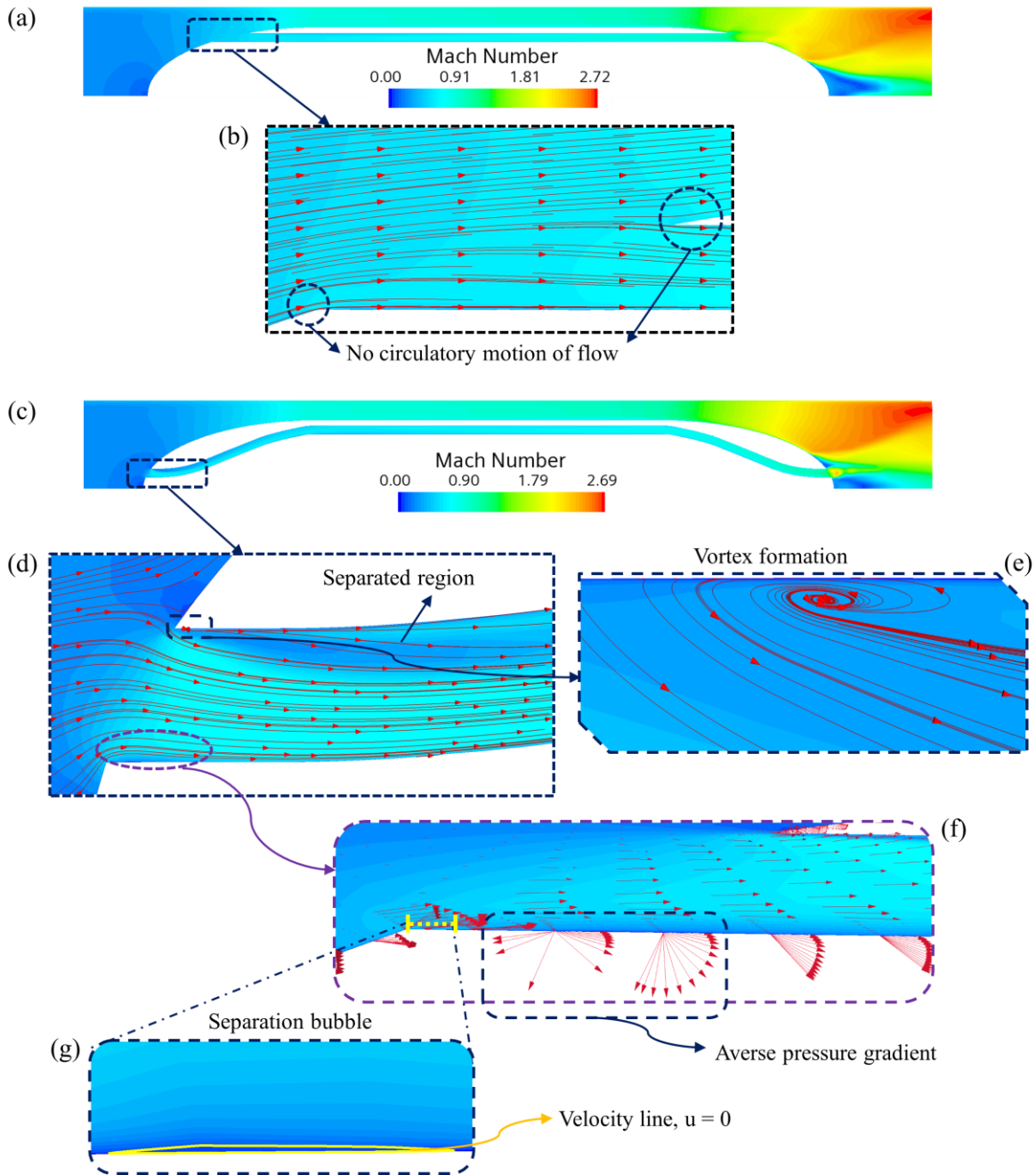


Fig. 14. Comparison of the flow structure within the top VD at $Ma = 0.6$ for DS type 1 and 4. (a) Mach distribution around design 6.1. (b) Streamlines at the VD's inlet showing no circulation occurred at the entrance. (c) Mach distribution around design 6.4. (d) Illustration of separated regions and streamlines at VD's inlet. (e) Magnified view of the rectangular box on VD's upper wall at the vicinity of the duct inlet displaying vortex formation by drawing streamlines. (f) Magnified view of the oval box on VD's lower wall showing the change in velocity vectors direction du to adverse pressure gradient. (g) Demonstration of separation bubble by drawing the velocity line ($u = 0$). Model configurations are labeled as referenced in Table 2.

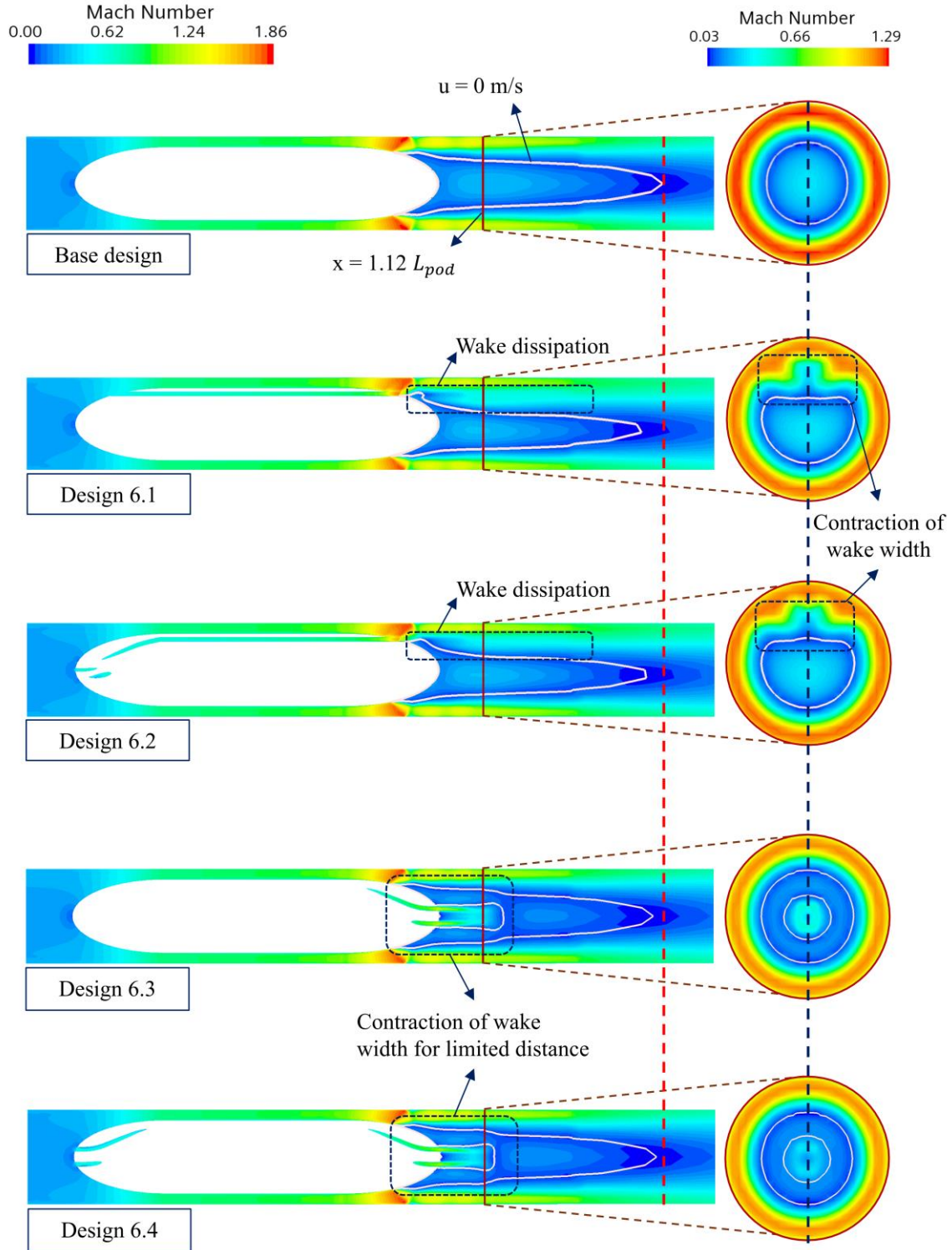


Fig. 15. Effect of different design strategies on wake region at $Ma = 0.4$; displaying Mach distribution around the pod for base pod model and for new designs with different arrays of VDs with six number of ducts. Model identifications are labeled below each contour, as listed in Table 2. The red dashed line compares the wake length between different cases, measured by the velocity line $u = 0$ (where u is the velocity component in the x -direction). Cross-sectional planes in the y - z direction used to illustrate Mach number distribution, positioned at a longitudinal distance of $1.12 L_{pod}$ downstream from the pod nose.

Further investigation was followed by comparing momentum coefficient of the discharged flow for each DS in Fig. 13(b). As expected, the maximum flow momentum was transferred

by design 6.1 and the lowest was for 6.4, confirming that efficiency of the VDs is highly dependent on their capability in convection of flow momentum. However, a distinct point exists between the graphs shown in Fig. 11(b) and Fig. 13(b). Despite achieving a drag reduction rate similar to 6.1, design 6.2 transferred lower momentum than 6.1 and even fell below 6.3 for $Ma \geq 0.4$. This indicates that another factor, aside from momentum of the duct outflow, influenced the reduction of C_{dp} for the tail.

As mentioned earlier, designs with identical duct outlets position provide similar drag reduction at the tail, indicating that there is a correlation between them. Fig. 16 depicts how each design changed the downstream flow field by drawing streamlines around the tail. The comparison focuses on designs 6.2 and 6.3, representing both position types for VD outlets. In the wake of the base model, two large vortices are observed, as shown in Fig. 16(b). The lower vortex is denoted by a brown dashed-dotted line. The interaction between these two vortices and the discharged flow can clarify how the outlet position of the ducts contributed to the more effective decay of wake vortices.

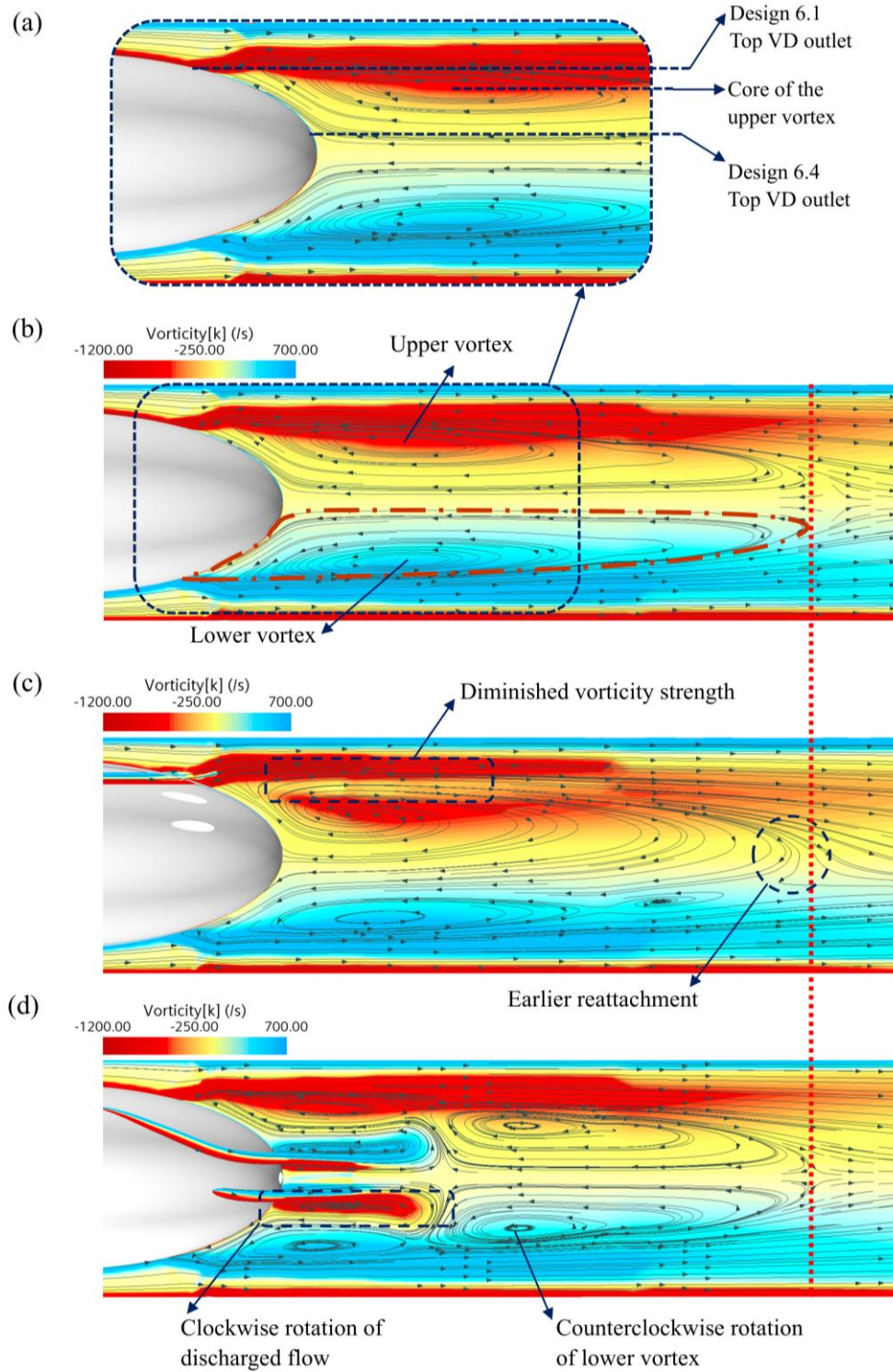
Design 6.2 has damaged the upper vortex structure, resulting in wake shrinkage and decreasing the extent of the area with strong vortical flow. This led to a decrease in its strength in creation of low-pressure region and earlier reattachment of the flow in the ending areas of the wake, as shown in Fig. 16(c). However, by design 6.3 wake was narrowed only for the area adjacent to the tail. The injected flow was in counter direction of vortices rotation causing the large vortices to split into smaller ones, as displayed in Fig. 16(d). While beyond a distance where injection was over, vortices with almost the same width exist.

This analysis reveals that two factors have contributed to a greater destruction of vortices and wake region. The radial distance of the duct outlets from core of the vortices shows a critical role in disruption of the wake. As illustrated in Fig. 16(a), in design 6.2 duct outlets are closer to the core of the upper vortex. Additionally, in this design, duct outlets are adjacent to the flow separation point on the pod tail, promoting earlier reattachment by adding extra momentum to the separated flow.

5.3. Influence of the number of ducts

The drag reduction results for configurations with 8 ducts ($N_d = 8$) can be compared with those for 6 ducts ($N_d = 6$), as presented in Table 4. There is a slight difference between them which is higher in low Mach numbers. Consistent with Section 5.2, the main contributors to

the pod drag, namely the pressure drag on the nose and tail, can be analyzed to explain why increasing N_d reduces the effectiveness of the VDs.



629

Fig. 16. Effect of different design strategies on wake vortices at $Ma = 0.4$ with demonstration of vorticity distribution and streamlines downstream of the pod. (a) Comparison of the duct outlets distance with core of the upper vortex. (b) Illustrating formation of two large vortices at the tail of the base pod design. (c), (d) Displaying effect of design 6.2, 6.3 on wake vortices. Model configurations are labeled as shown in Table 2. The red dotted line compares the end of recirculation in wake region for base model and designs 6.2 and 6.3.

In Section 5.2.1, the flow momentum drawn by the duct inlets is found to directly affect the reduction rate of nose pressure drag. As a result, the momentum coefficients measured at the VD inlets for DS Type 1 with 6 and 8 ducts are compared in Fig. 17(a). An increased number of ducts results in a lower momentum intake at each VD inlet. Further analysis shows that the intake flow velocity for designs with 8 ducts decreases by approximately 4.5% to 6%, depending on the free-stream Mach number, compared to those with 6 ducts. Since momentum is proportional to the square of velocity, the momentum for $N_d = 8$ is reduced by approximately 9.5% to 12%, as indicated in Fig. 17(a).

Fig. 17(b), 17(c) illustrate the effect of the number of ducts on the pressure distribution over the pod tail and the flow structure downstream of the pod for designs 6.1 and 8.1. Both designs exhibit increased pressure on the tail surface downstream of the VD outlets, as shown in Fig. 17(b). The difference in effectiveness between the 6-duct and 8-duct configurations is particularly evident in the vicinity of the duct outlets. As discussed earlier in this section, the VDs in design 6.1 receive higher momentum at their inlets compared to those in design 8.1. Therefore, it can be inferred that the 6-duct configuration has a greater capacity for pressure recovery in the wake region.

The visualization of the wake region for the 6-duct and 8-duct designs is consistent with this outcome. Although design 8.1 narrows the wake width, it does not enhance pressure recovery as effectively as design 6.1, as illustrated in Fig. 17(c) through both x - y and y - z cross-sectional planes. This is attributed to the lower momentum received at the duct inlets in design 8.1, resulting in less effective base pressure augmentation compared to design 6.1. Due to the similar qualitative behavior observed in the (6.2, 8.2), (6.3, 8.3), and (6.4, 8.4) configurations, their corresponding comparisons are provided in Supplementary Material (Appendix E). In conclusion, designs with a greater number of ducts were not only less effective in reducing pressure drag, but also increased skin-friction drag due to the additional duct surface area, leading to a lower overall drag reduction.

Increasing N_d in the Hyperloop pod design is beneficial as it provides more diagonal space for passengers and pod components. However, increasing N_d also results in smaller duct diameters to maintain the same removed frontal area. It was confirmed that the efficiency of the VDs depends on their diameter. Therefore, the number of ducts should be determined by balancing the trade off between maximizing internal space and minimizing power consumption.

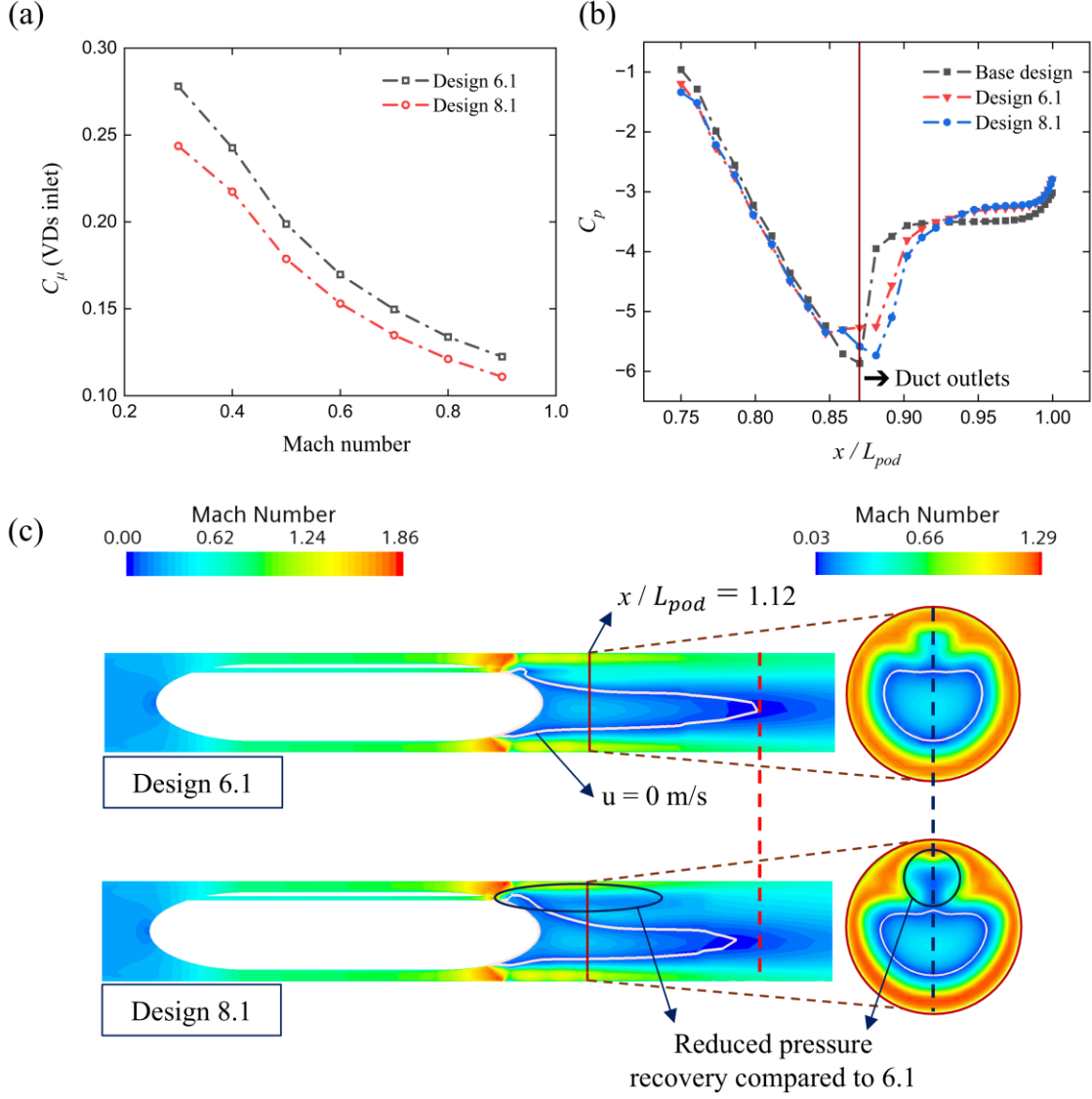


Fig. 17. Comparison of flow quantities between configurations using DS type 1 with 6 ducts (design 6.1) and 8 ducts (design 8.1). Model identifications are provided in Table 2. (a) Variation of the momentum coefficient at the VDs inlet across a wide range of Mach numbers, demonstrating the influence of the number of ducts (N_d) on intake flow characteristics. (b) Pressure coefficient profiles at the pod tail at $Ma = 0.4$, showing a stronger pressure rise near the duct outlets for the configuration with fewer ducts ($N_d = 6$). (c) Mach number distribution downstream of the pod tail at $Ma = 0.4$, shown on both the x - y and y - z cross-sectional planes. Results illustrate reduced pressure recovery in the wake with increased N_d (i.e., in design 8.1). The white line represents the location where the streamwise velocity component is zero ($u = 0$), used to compare wake length. The red dashed line indicates the influence of N_d on wake extent.

5.4. Maximum drag reduction

Previous sections analyzed the impact of various design parameters on the efficiency of the VD method. As shown in Table 4, a clear trend emerges, indicating that the drag reduction rate increases for all designs as the Mach number approaches 0.3. This section explores this repetitive influence on the pod drag reduction rate by explaining two external factors, outlined as follows.

5.4.1. Choking around the pod

Mach number of 0.3 is the closest to the choking condition. The choking condition is determined by the critical Mach number (Ma_{cr}), which is 0.26 in the present study, as explained in Section 5.1. As an initial prediction, it was proposed that the closer the free-stream Mach number is to the Ma_{cr} , the greater drag reduction is achieved. The results of the simulations were consistent with this hypothesis since for $Ma = 0.26$, drag reduction for all designs was the highest (e.g. for design 6.1, the calculated drag reduction was 16.3%, which is 4% higher than that for $Ma = 0.3$).

This phenomenon can be explained by the contributions of two factors. First, the occurrence of choking around the pod plays a pivotal role in this issue. As discussed in Section 5.1, choking causes airflow accumulation in front of the pod. Besides that, the critical Mach number marks the point at which airflow accumulation begins, i.e. the accumulated air is of lower intensity compared to the higher Mach numbers. This allows VDs to transfer more of the accumulated air from the pod front. At critical Mach number, VDs' capability is such that they even prevent choking and also eliminate the normal shock wave that would otherwise occur at the throat, as depicted in Fig. 18.

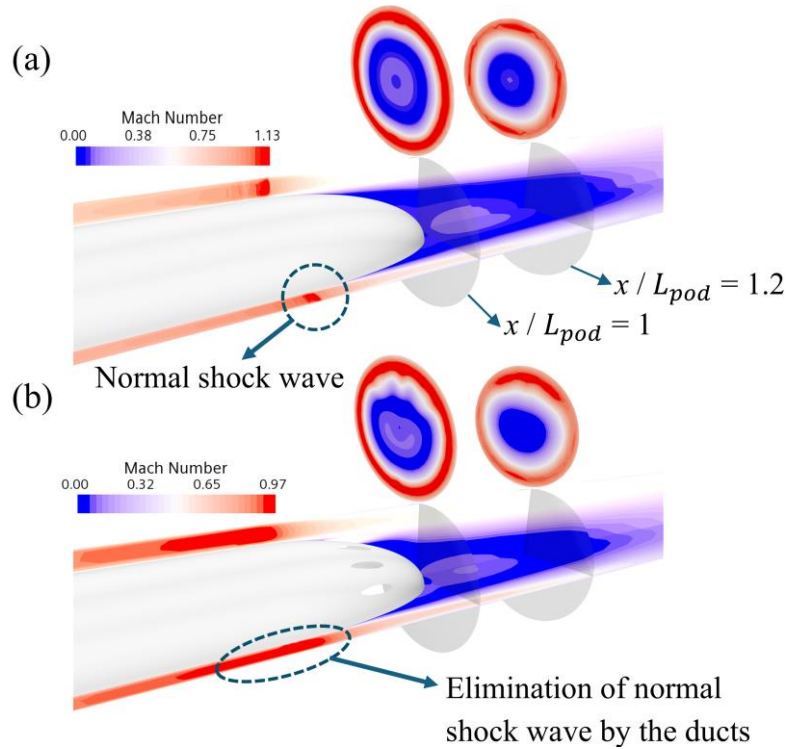


Fig. 18. Mach number distribution downstream of the pod on x-y plane ($z = -0.1$) and x-z plane ($y = 0$) at the critical Mach number ($Ma = 0.26$) for (a) the base pod model and (b) design 6.1. The comparison highlights the prevention of choking and the elimination of normal shock wave by the utilization of VDs. Cross-sectional planes are located at longitudinal positions of L_{pod} and $1.2L_{pod}$ from the pod nose. Model configurations are specified in Table 2.

5.4.2. Choking inside the ventilation ducts

The second factor influencing the achievement of maximum drag reduction at Ma_{cr} is related to the occurrence of choking inside the ventilation ducts. An analysis of duct flow reveals that flow inside the ducts become choked at $Ma = 0.4$. Fig. 19 shows the Mach number distribution along the top VD in design 6.1. It indicates that for $Ma \geq 0.4$ the flow Mach number inside the duct reaches 1 near the duct outlet, suggesting that the ducts operate at their maximum mass flow rate at these free-stream Mach numbers. This implies that the ducts ability to transport momentum do not increase linearly with the Mach number, leading to a reduced drag reduction rate as the Mach number increased.

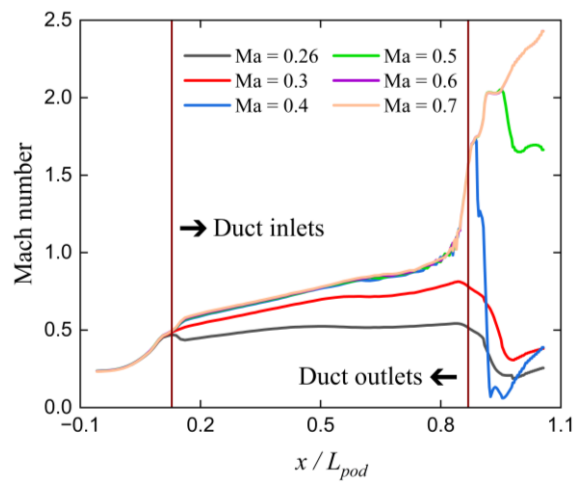


Fig. 19. Mach number distribution along the top VD in design 6.1 at various free-stream Mach numbers, illustrating the onset of choking within the duct for $Ma \geq 0.4$. The brown lines indicate the positions of the duct inlets and outlet on the pod. Model identification is specified as listed in Table 2.

Based on the discussions in Sections 5.4.1 and 5.4.2, the following summary can be presented. The VDs efficiency in drag reduction exhibits two distinct behaviors based on the free-stream Mach numbers.

1. For the Mach number range $0.26 \leq Ma < 0.4$, the mass flow rate (\dot{m}) through the ducts increases as a result of the higher flow velocity towards the pod. The rise in \dot{m} enhances the momentum. However, it is not compatible with the corresponding increase in pressure accumulation in front of the pod. Consequently, this mismatch decreases drag reduction rate at higher Mach numbers.
2. From $Ma = 0.4$ onwards, despite flow choking within the ducts, transferred momentum through the ducts is still increased due to elevated upstream flow density, which results from higher pressure accumulation in front of the pod. Additionally, ducts capability in transfer of mass flow reaches its maximum as the flow inside the ducts become choked.

As a result for $Ma \geq 0.4$, a specified portion of momentum, corresponding to the increased accumulated pressure in front of the pod, is transported to the wake. This aligns with the observed variation in the drag reduction rate at the pod nose, as illustrated in Fig. 11(a). The results indicate that from $Ma = 0.4$ onward, the rate of reduction in C_{dp} becomes nearly imperceptible.

According to this summary, drag reduction is not influenced only by the flow transfer rate and it should be evaluated with regard to the accumulated pressure in front of the pod. To compare ducts effectiveness under different circumferential conditions around the pod, a non-dimensional efficiency coefficient (C_e) is defined. It represents the fraction of the momentum ($\dot{m}v$) captured by the ducts, normalized by the product of the total pressure (P_t) upstream of the pod and the bypass area (A_{bypass}), as expressed in Eq. (3). It quantifies the effectiveness of the ducts in extracting momentum from the high-pressure buildup ahead of the pod. The upstream total pressure is measured by averaging over the y-z cross-sectional plane located $0.23L_{pod}$ ahead of the pod nose. The calculated values of C_e for design 6.1 at various Mach numbers are shown in Fig. 20. At critical Mach number ($Ma = 0.26$), where the maximum drag reduction is recorded, C_e has the highest value.

$$C_e = \frac{\dot{m}v}{P_t A_{bypass}}. \quad (3)$$

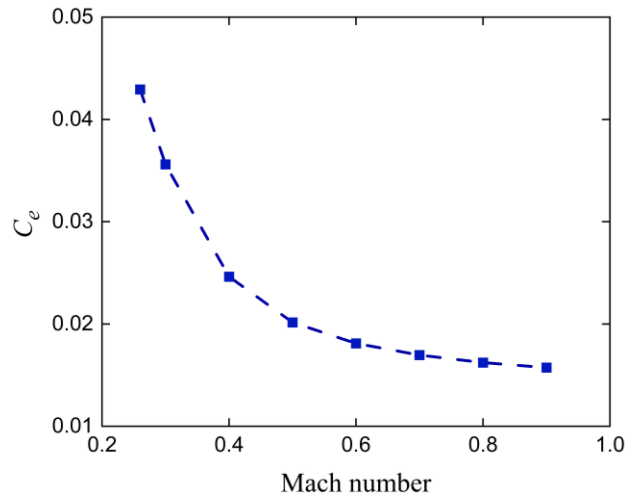


Fig. 20. Non-dimensional efficiency coefficient at different Mach numbers for design 6.1, representing the effectiveness of the ventilation ducts (VDs) in reducing pod drag under choking conditions ($Ma \geq Ma_{cr}$). The gradient of C_e highlights changes in duct efficiency as the Mach number increases. Model identification is labeled as referenced in Table 2.

Furthermore, it decreases sharply up to $Ma = 0.4$, the free-stream Mach number beyond which the flow becomes choked inside the ducts. Further increases in pod speed show that the gradient

of C_e does not change significantly. The variation of this parameter across different Mach numbers supports the findings presented in Section 5.2.1.

5.5. Comparison of ventilation ducts and compressor

In this section, we argue that employing VDs offers a more effective solution for reducing power consumption compared to the utilization of a compressor in the Hyperloop system. A comparison is made between the results of using VDs (obtained in the present study) and those from a compressor [70], in terms of reduction in total power consumption (P_{tot}). The blockage ratio of 0.72 is chosen for this purpose. To accomplish a correct comparison, the removed frontal area for both methods should be equal. Thus, similar to the previous study, 20% of the pod frontal area was considered for VD inlets. DS Type 1, identified as the optimal design strategy in this study, with $N_d = 14$, is employed for the comparison. Fig. 21 illustrates the corresponding design geometry. Efficiency of the both methods is evaluated by calculating the power coefficient (C_{power}) from Eq. (4), where ρ is the density of the air inside the tube, u is pod speed, A_f is the pod frontal area and P_{tot} represents the total power required for both the compressor and the propulsion system [70]. However, in the present study, no compressor is implemented in the pod model. Consequently, P_{tot} represents only the power required for the propulsion system which is equal to the total drag of the pod.

The results of the comparison are presented in Fig. 12. The reduction in P_{tot} obtained by the compressor for pod speeds up to Mach number of 0.6 is at least 15% and at most 40% lower than that of achieved by VDs. The results in this section indicate that the pressure of the accumulated air in front of the pod is sufficient to drive the airflow through the ducts without requiring additional power, eliminating the need for a compressor.

$$C_{power} = \frac{P_{tot}}{1/2 \rho u^3 A_f}. \quad (4)$$

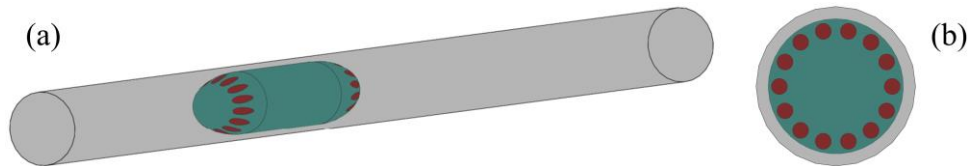


Fig. 21. (a) Three-dimensional (3D) view and (b) frontal view of the pod and tube for DS type 1 with 14 ducts, configured to maintain the same removed frontal area as the compressor model. This allows isolation of the effect of frontal blockage on flow behavior and aerodynamic drag.

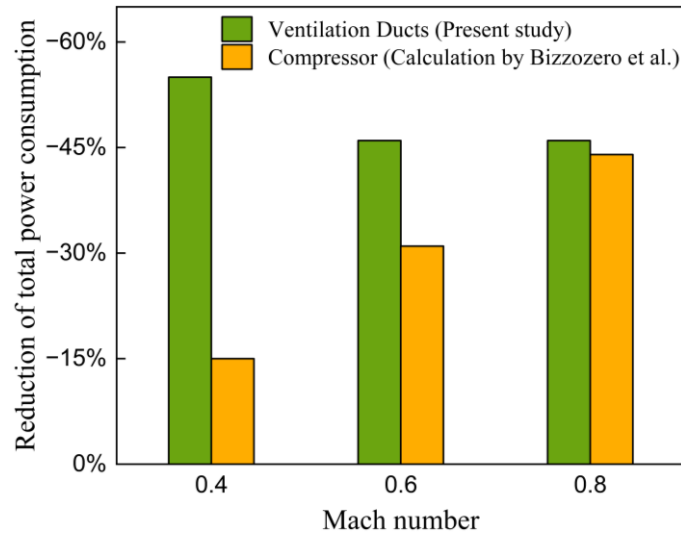


Fig. 22. Comparison of ventilation duct efficiency with compressor performance in reducing total power consumption of Hyperloop pod at Mach numbers 0.4, 0.6, and 0.8.. The results for the ventilation ducts are obtained in the present study, while compressor data are extracted from the study conducted by Bizzozero et al. [70].

Based on the findings of both the present and previous studies, it can be concluded that utilization of a compressor is entirely disadvantageous compared to the use of VDs. Foremost, employment of a compressor requires an external energy source, which increases power consumption of the Hyperloop system. Thus, in contrast to the VD method, the compressor not only failed to reduce power usage at low Mach numbers but also led to an increase in total power consumption [70]. Despite the compressor acceptable performance at higher Mach numbers, it remained remarkably less efficient than VDs. Even at $Ma = 0.8$, for which they have similar efficiency, the employment of a compressor has the drawback of occupying a significant space of the pod. While preserving the pod internal space is crucial rooted in the fact that the need for more space increases the pod size. This, in turn, raises the BR when the tube size is kept constant. As the BR increases, pressure accumulation in front of the pod becomes more severe leading to an increase in P_{tot} .

Additionally, the previous study overestimated compressor's capability in reduction of power consumption by unrealistically transferring airflow through a duct positioned within the pod center which is allocated for the passenger seat. As demonstrated in Section 5.2, location of the pathway for airflow transfer considerably affects both drag reduction and power consumption. Consequently, if simulations of the design involving an axial compressor were conducted along with practical transfer of airflow through the pod, the differences between these two approaches would be intensified.

6. Conclusion

In this study the efficiency of the ventilation duct (VD), as a passive drag reduction method, was investigated by the objective of decreasing power consumption of the Hyperloop pod. This analysis, for the first time, examines airflow passage through the pod body while keeping the passageway separate from the cargo and passenger compartments. Four design strategies (DS) for duct pathways and two values for the number of ducts (N_d) were considered, making eight different VD arrays, which occupy only 10% of the diagonal space of the passenger compartment. Through three-dimensional (3D) numerical simulations, the effectiveness of the VD method and the impact of each of design parameters, DS and N_d , on aerodynamic drag of the pod were evaluated.

It was revealed that DS type 1, in which ducts are conducted completely straight from the nose to the tail of the pod, provided the greatest drag reduction at various pod Mach numbers (Ma) ranging from 0.2 to 0.9. Contrary to the initial hypothesis that DS type 2 and 4 by which ducts take flow from a high-pressure region, stagnation point, were expected to reduce the nose pressure drag more effectively, instead design strategies featuring streamwise ducts, DS type 1 and 3, were more efficient. Momentum coefficient (C_μ) was chosen as the assessment parameter of VDs performance. The rotational path of ducts in DS types 2 and 4 resulted in flow separation on the internal wall of the VDs which led to confinement of mass flow rate and lower transference of momentum through the ducts. Consequently, at each pod speed, the DS elevating momentum transfer reduces pressure drag of the nose more efficiently.

Drag reduction of the tail part was affected by two factors including momentum transfer rate and position of the duct outlets while the second one had more significant impact, i.e., the DS in which duct outlets are positioned closer to the core of the wake vortices operated more effectively in disrupting them. This leads to boost recovery of pressure loss and higher reduction of drag as well. Hence, despite the higher injected momentum by DS type 3, it has decreased pressure drag of the tail part less than DS type 2 due to the position of duct outlets.

A comparison of the results for six and eight ducts brought us to this conclusion that increasing the number of ducts slightly decreases drag reduction. Nevertheless, adding more ducts results in a smaller diameter bringing down the efficiency of the ducts in transference of momentum. This, in turn, causes a drop in the reduction of pod pressure drag. However, constructing thinner VDs could help preserve more diagonal space within the pod. Therefore,

it was suggested that this parameter should be assessed regarding the priority of providing more space or less power consumption.

The maximum drag reduction exactly happened at critical Mach number (Ma_{cr}), that was 0.26 in this investigation. Two factors contributed to this phenomenon. First, by the occurrence of choking, the air mass starts to accumulate in front of the nose. Since a Mach number of 0.26 is the lowest speed at which the flow becomes choked, the accumulated air is less intense compared to flows at higher Mach numbers. As a result, at Ma_{cr} , VDs transferred a greater portion of the accumulated air from the upstream region of the pod, leading to a greater reduction in pressure drag.

Second, for $Ma \geq 0.4$, as the pod speed increased, the gradient of pressure drag reduction decreased, due to flow choking within the ducts. Accordingly, a higher airflow transfer rate through the VDs was not achievable at higher pod speeds. This implies that as the Mach number increased, the momentum transfer rate did not rise proportionally to the pressure accumulation in front of the pod. Consequently, a decrease in the rate of pressure drag reduction is reasonable. Through investigation of the results for reduction of pressure drag it was deduced that the efficiency of the ducts at different Mach numbers could be evaluated by considering their efficiency in the transport of momentum regarding the circumferential conditions that pod encountered. Ultimately, the ratio of the momentum captured by the ducts—normalized by the product of the upstream flow's total pressure and the bypass area—was recommended as the assessment parameter for efficiency of VDs in drag reduction. Variation of this parameter across all speeds was consistent with the change in drag reduction rate.

One of the most significant outcomes of this research is the comparison of the VD method and compressor. It was revealed that by utilization of VDs, a higher reduction in total power consumption can be obtained. Concerning this result and the lower occupation of pod space in comparison to the compressor makes this approach more advantageous.

Despite providing a more realistic flow transfer in this research, there are still deficiencies in the utilization of VDs as a practical approach. However, this was an attempt to make this transportation technology one step closer to exploitation.

References

- [1] Y. Zhang, D. Oster, M. Kumada, J. Yu, and S. Li, "Key vacuum technology issues to be solved in evacuated tube transportation," *Journal of Modern Transportation*, vol. 19, pp. 110-113, 2011.
- [2] M. Janić, "Future advanced long-haul Evacuated Tube Transport (EET) system operated by TransRapid Maglev (TRM): a multidimensional examination of performance," *Transportation Planning and Technology*, vol. 42, no. 2, pp. 130-151, 2019.
- [3] P. Beckert, G. Pareschi, J. Ehwald, R. Sacchi, and C. Bauer, "Fast as a plane, clean as a train? Prospective life cycle assessment of a hyperloop system," *Resources, Environment and Sustainability*, vol. 17, p. 100162, 2024.
- [4] D. Radeck *et al.*, "Case Study of an Integrated Design and Technical Concept for a Scalable Hyperloop System," *Applied System Innovation*, vol. 7, no. 6, p. 113, 2024.
- [5] D. Oster, "Evacuated tube transport," *USA Patent*, no. 5,950,543, 1999.
- [6] D. Oster, M. Kumada, and Y. Zhang, "Evacuated tube transport technologies (ET3) tm: a maximum value global transportation network for passengers and cargo," *Journal of Modern Transportation*, vol. 19, pp. 42-50, 2011.
- [7] E. Musk, "Hyperloop alpha," *SpaceX: Hawthorne, CA, USA*, 2013.
- [8] K. Decker *et al.*, "Conceptual feasibility study of the hyperloop vehicle for next-generation transport," 2017.
- [9] L. Mitropoulos, A. Kortsari, A. Koliatos, and G. Ayfantopoulou, "The Hyperloop System and Stakeholders: A Review and Future Directions," *Sustainability*, vol. 13, no. 15, p. 8430, 2021.
- [10] Z. Shen, "On developing high-speed evacuated tube transportation in China," *Journal of Southwest Jiaotong University*, vol. 40, no. 2, pp. 133-137, 2005.
- [11] J. C. Chin and J. S. Gray, "Open-source conceptual sizing models for the hyperloop passenger pod," in *56th AIAA/ASCE/AHS/ASC Structures, Structural Dynamics, and Materials Conference*, 2015, p. 1587.
- [12] K.-W. Wang *et al.*, "Formation and propagation characteristics of a weak shock wave in maglev tube," *Physics of Fluids*, vol. 36, no. 3, 2024.
- [13] S. Han *et al.*, "Influence of high-speed maglev train speed on tunnel aerodynamic effects," *Building and Environment*, vol. 223, p. 109460, 2022.
- [14] K. Wang *et al.*, "A two-dimensional revolving-axisymmetric model for assessing the wave effects inside the railway tunnel," *Journal of Wind Engineering and Industrial Aerodynamics*, vol. 248, p. 105716, 2024.
- [15] H. Guo, K. Zhang, G. Xu, and J. Niu, "Effects of pressure waves on the cooling-fan performance and indoor flow of air-conditioning units on the roof of a high-speed maglev train," *Tunnelling and Underground Space Technology*, vol. 145, p. 105608, 2024.
- [16] K. S. Jang, T. T. G. Le, J. Kim, K.-S. Lee, and J. Ryu, "Effects of compressible flow phenomena on aerodynamic characteristics in Hyperloop system," *Aerospace Science and Technology*, vol. 117, p. 106970, 2021.
- [17] T. Mrazek, Y. Sato, M. A. Sayed, and N. Nick, "Investigation of shock waves reflected at the end of a Hyperloop tube," *Aerospace Science and Technology*, vol. 139, p. 108379, 2023.
- [18] Z. Hou, Y. Zhu, J. Bo, and J. Yang, "A quasi-one-dimensional study on global characteristics of tube train flows," *Physics of Fluids*, vol. 34, no. 2, 2022.

- [19] S. Zhong, M. Yang, B. Qian, T. Wang, F. Wu, and L. Zhang, "Temporal evolution of flow field structure for vehicles accelerating in evacuated tube transportation system," *Physics of Fluids*, vol. 35, no. 2, 2023.
- [20] Q. Yu, X. Yang, J. Niu, Y. Sui, Y. Du, and Y. Yuan, "Theoretical and numerical study of choking mechanism of fluid flow in Hyperloop system," *Aerospace Science and Technology*, vol. 121, p. 107367, 2022.
- [21] F. Lluesma-Rodríguez and S. Hoyas, "Approximation of the Couette-Poiseuille flow on an annular domain in compressible regime for a hyperloop pod," *Results in Engineering*, vol. 21, p. 101680, 2024.
- [22] Z. Zhang, Y. Wang, G. Wang, F. Li, D. Wang, and J. Luo, "Aerodynamic energy consumption analysis of divided evacuated tube transportation system," *Engineering Applications of Computational Fluid Mechanics*, vol. 19, no. 1, p. 2454296, 2025.
- [23] J. Kim, T. T. G. Le, M. Cho, and J. Ryu, "Theoretical and numerical analysis of effects of sudden expansion and contraction on compressible flow phenomena in Hyperloop system," *Aerospace Science and Technology*, vol. 126, p. 107587, 2022.
- [24] Y. Seo, M. Cho, J. Ryu, and C. Lee, "Effects of branched tube on pressure waves in the hyperloop system: An experimental study," *Journal of Wind Engineering and Industrial Aerodynamics*, vol. 254, p. 105902, 2024.
- [25] J. Kim, K. S. Jang, T. T. G. Le, K.-S. Lee, and J. Ryu, "Theoretical and numerical analysis of pressure waves and aerodynamic characteristics in Hyperloop system under cracked-tube conditions," *Aerospace Science and Technology*, vol. 123, p. 107458, 2022.
- [26] J. Kim *et al.*, "Effects of eccentricity in tube-pod arrangements on hyperloop aerodynamics," *International Journal of Mechanical Sciences*, vol. 279, p. 109505, 2024.
- [27] A. J. Lang, D. P. Connolly, G. d. Boer, S. Shahpar, B. Hinchliffe, and C. A. Gilkeson, "Benchmark problems for simulating Hyperloop aerodynamics," *Physics of Fluids*, vol. 36, no. 10, 2024.
- [28] X. Hu, Z. Deng, J. Zhang, and W. Zhang, "Effect of tracks on the flow and heat transfer of supersonic evacuated tube maglev transportation," *Journal of Fluids and Structures*, vol. 107, p. 103413, 2021.
- [29] P. Zhou, D. Qin, J. Zhang, and T. Li, "Aerodynamic characteristics of the evacuated tube maglev train considering the suspension gap," *International Journal of Rail Transportation*, pp. 1-21, 2021.
- [30] N. Jiqiang, S. Yang, Y. QiuJun, C. Xiaoling, Y. Yanping, and Y. Xiaofeng, "Effect of acceleration and deceleration of a capsule train running at transonic speed on the flow and heat transfer in the tube," *Aerospace Science and Technology*, vol. 105, p. 105977, 2020.
- [31] P. Zhou and J. Zhang, "Aerothermal mechanisms induced by the super high-speed evacuated tube maglev train," *Vacuum*, vol. 173, p. 109142, 2020.
- [32] Q. Yu, X. Yang, J. Niu, Y. Sui, Y. Du, and Y. Yuan, "Aerodynamic thermal environment around transonic tube train in choked/unchoked flow," *International Journal of Heat and Fluid Flow*, vol. 92, p. 108890, 2021.
- [33] Q. Yu, X. Yang, J. Niu, Y. Sui, Y. Du, and Y. Yuan, "Thermal effects on the wall surfaces of transonic evacuated tube maglev transportation," *Applied Thermal Engineering*, vol. 222, p. 119876, 2023.
- [34] S. Bao, X. Hu, J. Wang, T. Ma, Y. Rao, and Z. Deng, "Numerical study on the influence of initial ambient temperature on the aerodynamic heating in the tube train system," *Advances in Aerodynamics*, vol. 2, pp. 1-18, 2020.

- [35] A. J. Lang, D. P. Connolly, G. de Boer, S. Shahpar, B. Hinchliffe, and C. A. Gilkeson, "A review of Hyperloop aerodynamics," *Computers & Fluids*, p. 106202, 2024.
- [36] Z. Zhou, C. Xia, X. Du, X. Shan, and Z. Yang, "Impact of the isentropic and Kantrowitz limits on the aerodynamics of an evacuated tube transportation system," *Physics of Fluids*, vol. 34, no. 6, 2022.
- [37] P. Zhou, J. Zhang, T. Li, and W. Zhang, "Numerical study on wave phenomena produced by the super high-speed evacuated tube maglev train," *Journal of Wind Engineering and Industrial Aerodynamics*, vol. 190, pp. 61-70, 2019.
- [38] Y. Seo, M. Cho, D. H. Kim, T. Lee, J. Ryu, and C. Lee, "Experimental analysis of aerodynamic characteristics in the Hyperloop system," *Aerospace Science and Technology*, vol. 137, p. 108265, 2023.
- [39] D. Radeck *et al.*, "Drag dependency aspects in Hyperloop aerodynamics," *Aerospace Science and Technology*, vol. 155, p. 109722, 2024.
- [40] Y. Sui, Q. Yu, J. Niu, X. Cao, X. Yang, and Y. Yuan, "Flow Characteristics and Aerodynamic Heating of Tube Trains in Choked/Unchoked Flow: A Numerical Study," *Journal of Thermal Science*, vol. 32, no. 4, pp. 1421-1434, 2023.
- [41] A. Kantrowitz, *Preliminary investigation of supersonic diffusers*. National Advisory Committee for Aeronautics, 1945.
- [42] Z.-D. Huang *et al.*, "Compressible effects of a supersonic evacuated tube maglev train at various Mach numbers," *Physics of Fluids*, vol. 36, no. 12, 2024.
- [43] Y. Sui, J. Niu, Q. Yu, Y. Yuan, X. Cao, and X. Yang, "Numerical analysis of the aerothermodynamic behavior of a Hyperloop in choked flow," *Energy*, vol. 237, p. 121427, 2021.
- [44] P. Zhou, J. Zhang, and T. Li, "Effects of blocking ratio and Mach number on aerodynamic characteristics of the evacuated tube train," *International Journal of Rail Transportation*, vol. 8, no. 1, pp. 27-44, 2020.
- [45] T.-K. Kim, K.-H. Kim, and H.-B. Kwon, "Aerodynamic characteristics of a tube train," *Journal of wind engineering and industrial aerodynamics*, vol. 99, no. 12, pp. 1187-1196, 2011.
- [46] J.-S. Oh *et al.*, "Numerical analysis of aerodynamic characteristics of hyperloop system," *Energies*, vol. 12, no. 3, p. 518, 2019.
- [47] S. Zhong *et al.*, "Investigation on flow field structure and aerodynamic load in vacuum tube transportation system," *Journal of Wind Engineering and Industrial Aerodynamics*, vol. 215, p. 104681, 2021.
- [48] H. Kang, Y. Jin, H. Kwon, and K. Kim, "A study on the aerodynamic drag of transonic vehicle in evacuated tube using computational fluid dynamics," *International Journal of Aeronautical and Space Sciences*, vol. 18, no. 4, pp. 614-622, 2017.
- [49] T. T. G. Le, K. S. Jang, K.-S. Lee, and J. Ryu, "Numerical investigation of aerodynamic drag and pressure waves in hyperloop systems," *Mathematics*, vol. 8, no. 11, p. 1973, 2020.
- [50] Y. Zhang, "Numerical simulation and analysis of aerodynamic drag on a subsonic train in evacuated tube transportation," *Journal of Modern Transportation*, vol. 20, no. 1, pp. 44-48, 2012.
- [51] Y. Sui *et al.*, "Impact of vacuum degree on the aerodynamics of a high-speed train capsule running in a tube," *International Journal of Heat and Fluid Flow*, vol. 88, p. 108752, 2021.
- [52] Z. Zhou, C. Xia, X. Shan, and Z. Yang, "Numerical Study on the Aerodynamics of the Evacuated Tube Transportation System from Subsonic to Supersonic," *Energies*, vol. 15, no. 9, p. 3098, 2022.

- [53] X. Hu, Z. Deng, J. Zhang, and W. Zhang, "Aerodynamic behaviors in supersonic evacuated tube transportation with different train nose lengths," *International Journal of Heat and Mass Transfer*, vol. 183, p. 122130, 2022.
- [54] H. Kim and S. Oh, "Shape optimization of a hyperloop pod's head and tail using a multi-resolution morphing method," *International Journal of Mechanical Sciences*, vol. 223, p. 107227, 2022.
- [55] T. T. G. Le, J. Kim, K. S. Jang, K.-S. Lee, and J. Ryu, "Numerical study on the influence of the nose and tail shape on the aerodynamic characteristics of a Hyperloop pod," *Aerospace Science and Technology*, vol. 121, p. 107362, 2022.
- [56] H. Wang, Y. Yang, M. Benedict, and D. Coleman, "Aerodynamic simulation of high-speed capsule in the Hyperloop system," in *35th AIAA Applied Aerodynamics Conference*, 2017, p. 3741.
- [57] J. Niu, Y. Sui, Q. Yu, X. Cao, Y. Yuan, and X. Yang, "Comparative numerical study of aerodynamic heating and performance of transonic hyperloop pods with different noses," *Case Studies in Thermal Engineering*, vol. 29, p. 101701, 2022.
- [58] J.-K. Choi and K.-H. Kim, "Effects of nose shape and tunnel cross-sectional area on aerodynamic drag of train traveling in tunnels," *Tunnelling and Underground Space Technology*, vol. 41, pp. 62-73, 2014.
- [59] X. Chen, L. Zhao, J. Ma, and Y. Liu, "Aerodynamic simulation of evacuated tube maglev trains with different streamlined designs," *Journal of Modern Transportation*, vol. 20, no. 2, pp. 115-120, 2012.
- [60] T. T. G. Le, J. Kim, M. Cho, and J. Ryu, "Effects of tail shapes/lengths of Hyperloop pod on aerodynamic characteristics and wave phenomenon," *Aerospace Science and Technology*, vol. 131, p. 107962, 2022.
- [61] Y. Sui, J. Niu, Q. Yu, X. Cao, Y. Yuan, and X. Yang, "Influence of vehicle length on the aerothermodynamic environment of the Hyperloop," *Tunnelling and Underground Space Technology*, vol. 138, p. 105126, 2023.
- [62] J. Braun, J. Sousa, and C. Pekardan, "Aerodynamic design and analysis of the hyperloop," *AIAA Journal*, vol. 55, no. 12, pp. 4053-4060, 2017.
- [63] M. M. Opgenoord and P. C. Caplan, "Aerodynamic design of the hyperloop concept," *Aiaa Journal*, vol. 56, no. 11, pp. 4261-4270, 2018.
- [64] N. Nick and Y. Sato, "Computational fluid dynamics simulation of Hyperloop pod predicting laminar-turbulent transition," *Railway Engineering Science*, vol. 28, no. 1, pp. 97-111, 2020.
- [65] W. Jia, K. Wang, A. Cheng, X. Kong, X. Cao, and Q. Li, "Air flow and differential pressure characteristics in the vacuum tube transportation system based on pressure recycle ducts," *Vacuum*, vol. 150, pp. 58-68, 2018.
- [66] X. Hu, Z. Deng, and W. Zhang, "Effect of cross passage on aerodynamic characteristics of super-high-speed evacuated tube transportation," *Journal of Wind Engineering and Industrial Aerodynamics*, vol. 211, p. 104562, 2021.
- [67] K. Zhou, G. Ding, Y. Wang, and J. Niu, "Aeroheating and aerodynamic performance of a transonic hyperloop pod with radial gap and axial channel: A contrastive study," *Journal of Wind Engineering and Industrial Aerodynamics*, vol. 212, p. 104591, 2021.
- [68] A. Li, H. Cui, Y. Guan, J. Deng, Y. Zhang, and W. Deng, "Study on Aerodynamic Drag Reduction by Plasma Jets for 600 km/h Vacuum Tube Train Sets," *Machines*, vol. 11, no. 12, p. 1078, 2023.
- [69] F. Lluesma-Rodríguez, T. González, and S. Hoyas, "CFD Simulation of a Hyperloop Capsule Inside a Low-Pressure Environment Using an Aerodynamic Compressor as Propulsion and Drag Reduction Method," *Applied Sciences*, vol. 11, no. 9, p. 3934, 2021.

- [70] M. Bizzozero, Y. Sato, and M. A. Sayed, "Aerodynamic study of a Hyperloop pod equipped with compressor to overcome the Kantrowitz limit," *Journal of Wind Engineering and Industrial Aerodynamics*, vol. 218, p. 104784, 2021.
- [71] J. Galindo, R. Navarro, B. Pallás, G. Torres, F. Lluesma-Rodríguez, and A. Antoranz, "Effect of operational pressure reduction on axial compressor performance by means of 3D CFD modeling at nominal operating speeds," in *Turbo Expo: Power for Land, Sea, and Air*, 2024, vol. 88056: American Society of Mechanical Engineers, p. V12AT29A015.
- [72] F.-R. Grosche and G. Meier, "Research at DLR Göttingen on bluff body aerodynamics, drag reduction by wake ventilation and active flow control," *Journal of Wind Engineering and Industrial Aerodynamics*, vol. 89, no. 14-15, pp. 1201-1218, 2001.
- [73] G. Meier, G. Suryanarayana, and H. Pauer, "Widerstandsverminderung durch Ventilation," *DGLR Bericht*, pp. 90-06, 1990.
- [74] "Ouvrage Alphetube– Collombey-Muraz– Rapport succinct pour information publique," *Eurotube*, 2019.
- [75] G. K. Suryanarayana, H. Pauer, and G. E. A. Meier, "Bluff-body drag reduction by passive ventilation," *Experiments in Fluids*, vol. 16, no. 2, pp. 73-81, 1993/12/01 1993, doi: 10.1007/BF00944909.
- [76] F.-R. Grosche, M. Lu, and H.-P. Kreplin, "Control of flow around bluff bodies by passive wake ventilation," in *New Results in Numerical and Experimental Fluid Mechanics IV: Contributions to the 13th STAB/DGLR Symposium Munich, Germany 2002*, 2004: Springer, pp. 140-147.
- [77] P. L. Roe, "Characteristic-based schemes for the Euler equations," *Annual review of fluid mechanics*, vol. 18, no. 1, pp. 337-365, 1986.
- [78] W. Rodi, "Experience with two-layer models combining the k-epsilon model with a one-equation model near the wall," in *29th Aerospace sciences meeting*, 1991, p. 216.
- [79] T.-H. Shih, W. W. Liou, A. Shabbir, Z. Yang, and J. Zhu, "A new k- ϵ eddy viscosity model for high reynolds number turbulent flows," *Computers & fluids*, vol. 24, no. 3, pp. 227-238, 1995.
- [80] S. Lardeau and F. Billard, "Development of an elliptic-blending lag model for industrial applications," in *54th AIAA aerospace sciences meeting*, 2016, p. 1600.
- [81] F. R. Menter, "Two-equation eddy-viscosity turbulence models for engineering applications," *AIAA journal*, vol. 32, no. 8, pp. 1598-1605, 1994.
- [82] N. Li, J.-T. Chang, K.-J. Xu, D.-R. Yu, W. Bao, and Y.-P. Song, "Prediction dynamic model of shock train with complex background waves," *Physics of Fluids*, vol. 29, no. 11, 2017.
- [83] M. Bauer, T. Grund, and W. Nitsche, "Experiments on active drag reduction on a complex outer wing model," *AIAA Journal*, vol. 53, no. 7, pp. 1774-1783, 2015.